ABSTRACT

Title of Document: CHARACTERIZING SMOKE DISPERSION ALONG BEAMED CEILINGS USING SALT-WATER MODELING

Chan Chau Siang, Master of Science, 2010

Directed By: Professor Andre Marshall,
Department of Fire Protection Engineering

The study successfully validated the use of salt-water analog modeling as an effective diagnostic, predictive and scaling tool for understanding fire dispersion in a beam-ceiling complex compartment using the Particle Image Velocimetry (PIV) and Planar Laser Induced Fluorescence (PLIF) techniques. Dimensionless dispersion signatures and front arrival times were compared between the fire and salt-water experiments which showed excellent agreement. Prediction of the detector lag times using fire and saltwater data agreed with that of fire experiments.

CHARACTERIZING SMOKE DISPERSION ALONG BEAMED CEILINGS USING SALT-WATER MODELING

By

Chan Chau Siang

Thesis submitted to the Faculty of the Graduate School of the
University of Maryland, College Park, in partial fulfillment
of the requirements for the degree of
Master of Science
2010

Advisory Committee:
Professor, Andre Marshall (Chair)
Professor, James G. Quintiere
Professor, Arnaud Trouvé

Acknowledgements

I would like to thank Defence Science and Technology Agency for sponsoring this MS program and the opportunity to pursue my interest in fire protecting engineering in University of Maryland. I am thankful of U.S. Department of Justice for sponsoring this project and also Bureau of Alcohol, Tobacco, Firearms, and Explosives, especially Dr. Dave Sheppard, for the collaboration on the full-scale tests.

My sincere thanks to the Dr. Arnaud Trouvé, James G. Quintiere and Dr. Andre Marshall for being in this advisory committee. A special thanks to Dr James G. for imparting his valuable knowledge in fire dynamics and fire scaling and has inspired me in this field. I am most thankful to Dr Andre Marshall for being my advisor throughout my course of this thesis work not only for his thoughtfulness, guidance, and knowledge but also his unrelenting patience in working through the problems with me. Thank you to Tom Layton for helping me so much in the preparing the salt-water experiments, and Allison Carey on the scaling program. Thank you to all fellow FPE friends for helping in one way or the other.

Finally, I am most grateful and appreciative of my wife, Sabrina for her unwavering love and support in my pursue of this MS course. And to my parents whom I am always indebted to, for the support, education and love that I have always received; as well as my sisters Vivian and Felicia for taking care of my parents when I am at oversea. I love you all!

Table of Contents

List of Tables

List of Figures

Nonmenclature

u_i plume mean velocity

T plume temperature

Q convective heat release rate $Q = \dot{Q}_c$

$\dot{m}_{salt}$ salt release rate

U_g characteristics velocity (buoyancy), $U_g \sim \left(\left|\rho_{source} - \rho_o\right| / \rho_o\right)^{1/2} (gL)^{1/2}$

U_c characteristic velocity (convection), $U_c \sim \left(\frac{Q}{\rho_o c_p T_o {L_f}^2}\right)\left(\frac{(T_{source} - T_o)}{T_o}\right)^{-1}$

U_o characteristic velocity, $= (gL_f)^{1/2}(Q^*)^{1/3}$ or $= (gL_{sw})^{1/2}(m_{sw}^*)^{1/3}$

τ_o characteristic flow time, $= (L_f / g)^{1/2}(Q^*)^{1/3}$ or $= (L_{sw} / g)^{1/2}(m_{sw}^*)^{-1/3}$

L_o characteristic length scale = L_f for fire or = L_{sw} for salt-water

L_f characteristic compartment height from virtual origin, z_0 for fire

L_{sw} characteristic compartment height from virtual origin, z_0 for salt-water

ρ_{source} source fluid density

ρ_0 ambient fluid density

T_0 ambient fluid temperature

c_p ambient fluid heat capacity

Y_{smoke} smoke mass fraction

Y_{salt} salt mass fraction

L_M Morton Length scale, $L_M = M^{3/4} / B^{1/2}$

B buoyancy flux, $= \frac{\rho_{source} - \rho_0}{\rho_{source}} g U_{inj} L_{inj}^2$

M momentum flux, $= U_{inj}^{1/2} L_{inj}^{1/2}$

t^* dimensionless time, $= t_f \, (L_f / g)^{-1/2} (Q^*)^{1/3}$ or $= t_{sw} (L_{sw} / g)^{-1/2} (m_{sw}^*)^{1/3}$

u_i^* dimensionless velocity, $= u_i (g L_f)^{-1/2} (Q^*)^{-1/3}$ or $= u_i (g L_{sw})^{-1/2} (m_{sw}^*)^{-1/3}$

$\dot{q}^*$ dimensionless volumetric energy release rate

$\dot{w}^*$ dimensionless volumetric species release rate

Q^* dimensionless source strength for fire, $Q^* = \beta_T Q / \rho_0 c_p g^{1/2} L_f^{\,5/2}$

m_{sw}^* dimensionless source strength for salt water, $m_{sw}^* = \beta_{sw} \dot{m}_{salt} / \rho_0 g^{1/2} L_{sw}^{\,5/2}$

Re Reynolds number

Re_D characteristic Reynolds number, $Re_D = UD / \upsilon$

Pr Prandtl number

Sc Schimidt number

Gr Grashof number, $= g \beta_T \dot{Q} L_f^{\,2} / \rho_0 c_p \upsilon^3$ for fire; $= g \beta_{sw} \dot{m}_{salt} L_{sw}^{\,2} / \rho_0 c_p \upsilon^3$ for salt

τ_d detector characteristic time constant

L_d detector geometric entry resistance

$Y_{smoke,i}$ smoke mass fraction inside detector

$Y_{smoke,ir}$ detector threshold

L_{ODM} optical path length of the optical density meter

[dye] mass concentration of dye

[salt] mass concentration of salt

[smoke] mass concentration of smoke

C_1 calibration parameter relating PLIF image intensity to dye concentration

C_2 calibration parameter relating dye concentration to salt concentration

Greek

υ kinematic viscosity

α thermal diffusivity

D mass diffusivity

ε extinction coefficient

β volumetric expansion coefficient, = $1/T_0$ for fire; = 0.76 for salt water

θ dimensionless density difference, $= \beta_T (T - T_0)$ for fire; $= \beta_{sw} Y_{salt}$ for salt-water

Subscript

$_{sw}$ salt-water

$_f$ fire

$_T$ thermal

$_{smoke}$ *smoke*

$_D$ *diameter of the source*

$_{inj}$ salt-water injector

$_{FA}$ front arrival

$_{lag}$ detector lag

$_{ACT}$ detector activation

Chapter 1: Introduction

Smoke inhalation has been the leading cause of death during fire accidents; and has led numerous researches being carried out to understand the dynamics of smoke movement and early smoke detection in effort to protect life and property.

Practical engineering purposes in the knowledge of the fire-induced ceiling flows include the design optimization of the placement of smoke and heat detectors, calculation of smoke movement, estimating the impacts of smoke toxicity on evacuations, and the prediction of heat transfer to the ceiling.

The pioneering works by Alpert[1,2], Delichatsios[3] and Heskestad[4,5] focused on empirical correlations for smoke movement along flat ceilings and the use of mathematical model to predict detector response time. Recent developments included the understanding of smoke movement in complex environments such as multi-compartments[6,7,8] and beamed ceilings configurations[9,10,11,12] on detection locations and sprinkler responses.

However, the approach to such difficult problems of beamed ceiling flows, which is complicated by awkward obstructions, is often studied using physical modeling or computer simulations. Hydraulic analog modeling using salt-water is an excellent tool for visualizing and quantifying the characteristics of smoke movement and fire induced flows. Successful quantitative validations of smoke dispersions using salt-

water scaling theory and advanced laser diagnostics motivated this research work on beamed ceilings in a complex geometry and possible applications for code validations and fire reconstructions.

The collaboration with Bureau of Alcohol, Tobacco, Firearms and Explosives (ATF) Fire Research Laboratory on this project enables the comparison of the results from the salt-water experiments using a $1/15^{th}$ scale model with the that of the full-scale fire experiments. This helps establish the theory and accuracy for the scaling used in the physical modeling.

Further to this, quantitative data extracted from the salt-water modeling experiments such as the front arrival times, the plume's velocity and dispersion concentrations are used to predict detector response based on the scaling theory and existing mathematical models developed for smoke detectors.

1.1 Motivation

Fire engineering analysis and modeling are becoming more commonplace for fire incident reconstruction. A treatise funded by U.S. Department of Justice was developed to document the theory, accuracy and limitations of physical scale modeling, as well as hydraulic analog scaling using salt-water. The key benefit will be the visualization, qualitative and quantitative analysis of the fire hypothesized with the savings of cost and time. Physical modeling has also the additional benefit of

modeling complex enclosures without loss of the real physics as the fire-induced flows are naturally mimic in the experiments. To validate the results from the scale modeling experiments, the results from ATF's full-scale fire tests involving a complex corridor compartment with beamed ceilings are used as the control.

Ceiling obstructions, such as beams, joists and miters can significantly affect the flow of the smoke along the ceiling. Despite many studies being carried out using full-scale tests and numerical field modeling, most works focused on the qualitative evaluation of smoke detector and sprinkler spacing requirements in various beamed ceiling configurations. Only few researches were carried out on correlating the dispersion profiles such as the temperature, velocity and smoke concentration, and are still not fully characterized for use in performance-based fire engineering designs. This research attempts to use salt-water analog modeling to provide some visualization for the complex beam-ceiling flows and present some quantitative results to enhance current practices.

The characterization of the smoke detector response is useful for many fire designs, including optimizing the placements of the smoke detectors for early smoke detection, fire design analysis, investigation, risk evaluations and product development. A practical approach is suggested in this paper to predict the smoke detector response based on the dispersion characteristics of the fire-induced flows. The predictions for the smoke detector response are then compared to the data in the actual fire experiments to validate the methodology. Through the use of scaling

theory, this research will also demonstrate the benefits of using the simulated dispersion results from the salt-water experiments as an engineering tool, in this case to predict the smoke detector response.

Other applications of salt-water modeling though not emphasized in this research can be useful to evaluate fire phenomenon such as smoke filling, vent flows, entrainment patterns and smoke toxicity analysis.

1.2 Literature Review

1.2.1 Salt-water Modeling

Physical scale modeling is commonly used in engineering fields to mimic the real physics of complex systems for design and analysis. Quintiere[13] developed the scaling techniques for fire studies using Froude modeling which preserve the velocity of the buoyancy-driven flow from the energy source. In a similar fashion, Steckler[6] et al. established the use of hydraulic analog scaling for fire-induced flows using salt-water modeling; and demonstrated the use of blue dye technique to visualize the analog fire dispersion in a $1/20^{th}$ scale model of a U.S. Navy Ship where both the smoke front arrival and layer height were discussed.

Many other researchers have used the salt-water technique as qualitative tools to evaluate smoke movement in multi-compartments and complex geometries. Thomas[14] et al showed the effect of vent flow from large rooms using salt-water. Zukoski[15] used

saltwater to predict the smoke movement in high-rise buildings. Zhang[16] combined salt-water simulation with double-liquid-dyeing technique for qualitative study of the characteristic movement of smoke and induced air in a corridor adjoining a room. Kelly[7] studied the analog dispersion within a two-storey compartment using conductivity probe at a specific location of interest, and found scaling agreement under different salt-water flow conditions.

In recent studies, quantitative analysis of the salt-water flow was carried out using the non-intrusive Particle Image Velocimetry (PIV) and Planar Laser Induced Fluorescence (PLIF) techniques for velocity and concentration measurements respectively. Clement and Fleischman[17] performed PLIF measurements of the salt-water flow in a two-room enclosure and validated the hydrodynamic model within Fire Dynamics Simulator (FDS). Jankiewicz[8] used the PLIF techniques to study the detector response times in a multi-compartment enclosure, and found excellent agreement for the dimensionless front arrival times in both saltwater and full-scale fire experiments. Young[18] used the PIV technique to study the plume dispersion near a building in a cross-flow environment. Yao[19,20,21] et al. presented a detailed analysis of the turbulent mixing and heat transfer in canonical fire plume configurations using quantitative salt-water measurements, with good agreement with the theory.

1.2.2 Ceiling Jets in Beam Ceiling Configurations

Several studies were carried using full-scale tests or numerical simulations to study the effect of ceiling configurations on ceiling jets, mainly because of the concerns on

delayed response of detectors and sprinklers. Taylor[22] first presented the impact of beams on flow of hot gases in 1912. The impact of open joisted ceiling on fire detectors was only compared in an experiment carried out National Board of Fire Underwriters in 1956. Following that, many more studies were carried at Factory Mutual by Heskestad and Delichatsios[23], Heskestad[24] on both detector and sprinkler response under beamed ceilings.

A model was proposed by Delichatsios[9] to predict the properties of beamed ceiling flow by describing a discontinuous flow over the beams involving a density jump from a high to low Froude number. Koslowski[10,12] investigated the effect of beam obstructions on an unconfined ceiling jet using small-scale experiments, which validated the empirical relation developed by Delichatsios and found a modified empirical relation for predict the ceiling jet velocity and temperature perpendicularly beyond the obstructions based on the ceiling heat transfer and the beam to ceiling height ratio. Motevalli[25] and Zheng expanded on Koslowski's work to predict the temperature and velocity of beamed ceiling flow along the centerline within the secondary bay.

Recent works have explored computational simulations to validate the results from the full-scale tests and have provided some understanding in beamed ceiling jet flows. Forney[11,26] et al simulated the flow of smoke under beam ceilings using numerical field modeling and demonstrated using the computed data to predict the temperature distribution in beamed ceilings and later used the predictions to evaluate detector and

sprinkler response. O'connor[27] performed Computational Fluid Dynamics (CFD) under FDS to evaluate smoke detector performance under a variety of flat beamed ceiling configurations. Floyd[28] extended the study for parallel beamed hallways and sloped ceilings. Mealy[29] subsequently performed an experimental validation of the computational simulation for the flat beamed ceilings, and found comparable flow properties when he compensated for the soot deposition on the beamed ceilings.

1.2.3 Spot-type Smoke Detector Response

It is well known that the time delay in spot-type smoke detector response is a direct result of the additional time required for the convective transport of the smoke into the detector sensing volume despite the threshold value being attained outside the detector housing. Many smoke detector response models based on activation criteria were proposed to predict this time delay, which is also known as the detector lag time.

Earlier models used surrogate methods to predict the detector lag time using either temperature-based or optical density-based correlation. The temperature rise analogy was initially proposed by Heskestad and Delichatsios[3] based on the range temperature rise observed in a series of full-scale smoke detector tests conducted at Factory Mutual and National Institute of Standards and Technology in late 1970s. The smoke detector was assumed to be activated when the gases in the vicinity of the smoke detector reached an average temperature rise of 13°C. Similar surrogate approach[30,31,32,33] based on increased light obscurations observed near the vicinity of

the detector was used to predict the detector lag time. However, such surrogate methods neither fully account for the physics of the sensing spot-type smoke detector technology, nor directly account for the detector lag time due to the buoyancy-induced flow.

More detailed studies were carried out later to account for the lag time by defining a detector characteristic time for the detector to reach the activation threshold when the gas in the vicinity of the detector had reached the activation threshold. Heskestad[5] proposed a first-order time response detector model relating the detector characteristic length to the gas velocity in the vicinity of the detector. The detector characteristic length, which was often found experimentally, was representative of the geometric features of the particular detector affecting the detector response. However, Bjorkman[34] et al found Heskestad's model limited to flow velocity more than 0.16m/s. Clearly[35] expanded on Heskestad's study by describing the entry lag using a characteristic dwell time and mixing time; where the dwell time described the time delay for the gas to enter the detector chamber and the mixing time describing the time for the gas to fill the detector chamber to the activation threshold. While the above detailed modeling provided a better understanding o the detector response, these lag time methods were less popular due to the lack of available critical design information such as the detector characteristic length, localized gas velocity and smoke concentration.

Previous investigations have demonstrated that salt-water modeling can be a useful tool in characterizing dispersion in fire induced flows. Hence, quantitative data on the dispersion velocity and concentration can be obtained using PIV and PLIF techniques, and it is possible to use salt-water modeling as a predictive tool for determining detector activation times provided that the modeled dispersion behavior in the vicinity of the detector can be appropriately related to the detector activation.

In addition, few other researches focused on addressing specific ionization detector response time based on chamber resistance depending on the electrode geometry, ion properties, smoke density and smoke particle size. However, many of these methods are still relatively new, and less widely used.

1.3 Research Objectives

This main purpose of this research is to establish the theory, accuracy and limitations of the physical analog scaling using salt-water modeling, which is applicable fire reconstruction, investigation, and fire design analysis.

Using advanced laser diagnostics, quantitative dispersion profiles of beam ceiling jets were investigated in an unprecedented way using salt-water modeling. The dimensionless dispersion measures were extracted from the salt-water experiment to validate existing detector response models for predicting detector activation times.

The specific objectives of this research are to:

- Develop and characterize a large source-based injector plume system for salt-water modeling
- Perform Blue Dye Salt-water, PIV and PLIF experiments to describe the dispersion characteristics qualitatively and quantitatively.
- Establish the theory, accuracy and limitations of physical analog scaling using salt-water modeling by comparing the quantitative dispersion salt-water experimental results with the ATF full-scale fire tests in a complex corridor compartment with beamed ceilings.
- Analyze qualitatively and quantitatively the dispersion characteristic of the buoyant plume along beamed ceiling using Blue Dye Visualization, PIV and PLIF techniques.
- Examine the use of salt-water modeling for determining the detector response time, and compare with actual test results.

Chapter 2: Approach

A series of full-scale fire experiments involving different fire source types were conducted at ATF while the small-scale fire and salt-water experiments were conducted at the University of Maryland (UMD) Fire Protection Engineering Laboratories to investigate the fire scaling methodologies.

Using the method of dimensionless analysis on the governing conservation equations, the dimensionless groups relating to the fire phenomena can be derived. In order to match the full-scale results with the small-scale modeling results, these dimensionless groups need to be preserved. While it is impossible to preserve all the dimensionless groups in reality, the art of scaling is then to cleverly select the key dimensionless variables best describing the fire phenomena without loss of generality of the flow through approximate formulas.

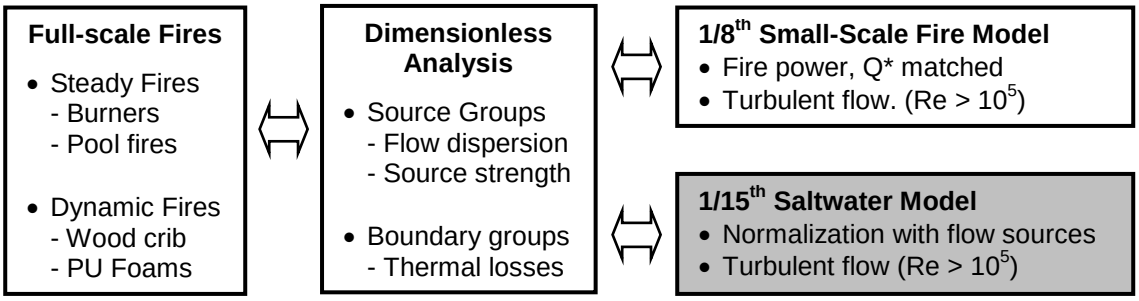

Figure 1 Overview of scaling approach

In practice, the Reynolds number is not specifically scaled, but preserved by maintaining the flow to be turbulent in both full-scale and small models, and a reference velocity representing for the convection and buoyancy is typically defined. This is done by considering the Froude number, the ratio of the velocities to be equal to one (i.e. $Fr = U_g / U_c = 1$). While it is common for the small-scale fire experiments to match the dimensionless fire power with the length scale to the power of 5/2, salt-water modeling incorporated in its equations the normalization of the fire power, thus allowing experiments of different source strengths to be compared.

This research work focused on the scaling comparisons with the burner sources and pool fires representing the steady fires. Blue dye visualizations of the salt-water dispersion were first carried out to select the flow sources and identify the key interest regions, before employing the PIV and PLIF techniques to quantify the specific regions of the flow. Dimensionless flow quantities were extracted from the salt-water experiments to compare with full-scale fire results.

2.1 Modeling Methodology

2.1.1 Fire-Salt-water Analog Modeling

Through similitude, the use of the dimensionless variables (superscript *) allows us to easily compare the source flow in different spaces and times. Yao[20] derived the scaling relationships between the salt-water model and full-scale fire by expressing the governing conservation equations in their dimensionless forms as shown below.

(i) Conservation equations for Fire Plume

Momentum:

$$\frac{\partial u_j^*}{\partial t^*} + u_i^* \frac{\partial u_j^*}{\partial x_i^*} = -\frac{\partial p^*}{\partial x_i^*} + \frac{1}{(Gr_{source}^{fire})^{1/3}} \frac{\partial^2 u_j^*}{\partial x_i^* \partial x_i^*} + \theta_T^* \cdot f_j^* \quad , \tag{2.1}$$

Energy:

$$\frac{\partial \theta_T^*}{\partial t^*} + u_i^* \frac{\partial \theta_T^*}{\partial x_i^*} = \frac{1}{(Gr_{source}^{fire})^{1/3} Pr} \frac{\partial^2 \theta_T^*}{\partial x_i^* \partial x_i^*} + q_T^* \quad , \tag{2.2}$$

Smoke mass species:

$$\frac{\partial \theta_{smoke}^*}{\partial t^*} + u_i^* \frac{\partial \theta_{smoke}^*}{\partial x_i^*} = \frac{1}{\left(Gr_{source}^{fire}\right)^{1/3} Sc} \frac{\partial^2 \theta_{smoke}^*}{\partial x_i^* \partial x_i^*} + w_{smoke}^* \tag{2.3}$$

where $Gr_{source}^{fire} = \dfrac{g\dot{Q}L_f^{\,2}}{\rho_o c_p T_o \upsilon^3} = \left(\mathrm{Re}_{source}^{fire}\right)^3 (Q*)$, $Pr = \dfrac{\upsilon}{\alpha}$, $Sc = \dfrac{\upsilon}{D}$

And the scaled variables in terms of the source terms were

$$t_f^* = t_f \left(g / L_f\right)^{1/2} \left(Q^*\right)^{1/3}, \; u_j^* = \frac{u_j}{\left(Q^*\right)^{1/3} \left(gL_f\right)^{1/2}}, \; \theta_T^* = \frac{\beta_T \left(T - T_o\right)}{\left(Q^*\right)^{2/3}},$$

$$\theta_{smoke}^* = \frac{\beta_T Y_{smoke} \Delta H_c}{\left(Y_{smoke}\right)_o c_p \left(Q^*\right)^{2/3}}, \; Q^* = \left(\frac{\beta_T \dot{Q}}{\rho_o c_p g^{1/2} L_f^{\,5/2}} \right)$$

where $\beta_T = \dfrac{1}{T_o}$.

(ii) Conservation equation for salt-water plume

Momentum:

$$\frac{\partial u_j^*}{\partial t^*} + u_i^* \frac{\partial u_j^*}{\partial x_i^*} = -\frac{\partial p^*}{\partial x_i^*} + \frac{1}{(Gr_{source}^{sw})^{1/3}} \frac{\partial^2 u_j^*}{\partial x_i^* \partial x_i^*} + \theta_{sw}^* \cdot f_j^*, \qquad (2.5)$$

Salt Mass Species:

$$\frac{\partial \theta_{sw}^*}{\partial t*} + u_i^* \frac{\partial \theta_{sw}^*}{\partial x_i^*} = \frac{1}{(Gr_{source}^{sw})^{1/3} Sc} \frac{\partial^2 \theta_{sw}^*}{\partial x_i^* \partial x_i^*} + \dot{\omega}_{sw}^*, \qquad (2.6)$$

where $Gr_{source}^{sw} = \dfrac{\beta_{sw} \dot{m}_{salt} g L_{sw}^2}{\rho_o \upsilon^3} == \left(\mathrm{Re}_{source}^{fire}\right)^3 \left(\dot{m}_{sw}^*\right),\ Sc = \upsilon / D$

And the scaled variables in terms of the source terms were

$$t_{sw}^* = \frac{t_{sw}}{\left(\dot{m}_{sw}^*\right)^{-1/3} \left(g / L_{sw}\right)^{-1/2}},\ u_j^* = \frac{u_j}{\left(g L_{sw}\right)^{1/2} \left(\dot{m}_{sw}^*\right)^{1/3}},$$

$$\theta_{sw}^* = \frac{\beta_{sw} Y_{salt}}{\left(\dot{m}_{sw}^*\right)^{2/3}},\ \dot{m}_{sw}^* = \frac{\beta_{sw} \dot{m}_{salt}}{\rho_o g^{1/2} L_{sw}^{5/2}}$$

where $\beta_{sw} = 0.76$.

The flows "not close" to the boundary were convective-buoyancy dominated; and hence the density deficit, $\left|\rho_{source} - \rho_o\right| / \rho_o$ of the flow may be expressed using an appropriate velocity scale due to gravity, U_g as given by

$$U_g \sim \left(\frac{\left|\rho_{source} - \rho_o\right|}{\rho_o}\right)^{1/2} (gL)^{1/2}. \qquad (2.7)$$

The other useful alternative of the velocity scale, U_c representing the convection of the heat, which was based on its source strength and temperature difference, may be expressed as

$$. U_c \sim \left(\frac{Q}{\rho_o c_p T_o L_f{}^2} \right) \left(\frac{(T_{source} - T_o)}{T_o} \right)^{-1} \tag{2.8}$$

Consider Boussinesq flow,

$$U_c \sim \left(\frac{Q}{\rho_o c_p T_o L_f{}^2} \right) \left(- \frac{(\rho_{source} - \rho_o)}{\rho_o} \right)^{-1} \tag{2.9}$$

Equating equation 2.8 and 2.9, the density deficit for the fire plume was simplified and expressed as

$$\frac{\rho_{source} - \rho_o}{\rho_o} \sim \left(Q^* \right)^{2/3} \tag{2.10}$$

Similarly, the velocity scale for the for the salt-water plume can derived from the convection of the salt-water mass flow and be expressed as

$$U_c \sim \left(\frac{\dot{m}_{salt}}{\rho_o L_{sw}^2} \right) \left(\frac{1}{\beta_{sw}} \right)^{-1} \left(\frac{(\rho_{source} - \rho_o)}{\rho_o} \right)^{-1} \tag{2.11}$$

And the density deficit for the saltwater plume was simplified as

$$\frac{\rho_{source} - \rho_o}{\rho_o} \sim \left(\dot{m}_{sw}^* \right)^{2/3} \tag{2.12}$$

Hence, a reference velocity with the information on its source strength was defined using Froude modeling and thus a corresponding characteristic flow time, $\tau_o = L_0 / U_o$ where L_o is the characteristic length scale.

Dynamic similarity was clearly demonstrated in both momentum equations for the fire and salt-water configurations. However, the discrepancies between governing dimensionless groups *Gr*, *Pr*, *Sc* in the energy and mass species equations between the fire and salt-water configurations may cause the flows to behave differently. Like all practical issues of modeling through scaling, it was not always possible to preserve all dimensionless groups, but to achieve useful results with good approximations.

When the *Gr* number was sufficiently large to create a turbulent flow in both configurations, the molecular diffusion would be relatively small compared to the turbulent mixing, and hence the associated dimensionless parameters may be neglected. Past studies[7,8,20] showed good agreement between the salt-water models and full-scale fires when *Gr* for the salt-water model exceeds 10^9 even though the Reynolds number, Re may be as low as 10^3.

However, near the boundary where the gradients of the velocity and temperature may be steep and hence the differences in *Gr*, *Pr* and *Sc* between the configurations may not be neglected. In addition, the impermeable boundary condition of the salt-water configuration causing zero mass loss at the wall is analogous to adiabatic boundary condition in the fire configuration.

Table 1 showed the independent dimensionless variables (i.e. time and position) and dependent dimensionless variables based on the source strengths for both fire and salt-water plume.

S/N	***Dimensionless Variables***	***Full-scale Fire***	***Salt-water Model***
(a)	*Dimensionless source strength parameter*	$Q^* = \beta_T Q(\rho_0 c_p g^{1/2} L_f^{5/2})^{-1}$ $\beta_T = 1/T_0$	$m_{sw}^* = \beta_{sw} \dot{m}_{salt} (\rho_0 g^{1/2} L_{sw}^{5/2})^{-1}$ $\beta_{sw} = 0.76$
(b)	*Dimensionless velocity, u**	$u_j^* = u_j (gL_f)^{-1/2} (Q^*)^{-1/3}$	$u_j^* = u_j (gL_{sw})^{-1/2} (m_{sw}^*)^{-1/3}$
(c)	*Dimensionless position, x**	$x_i^* = x_i / L_f$	$x_i^* = x_i / L_{sw}$
(d)	*Dimensionless time, t**	$t^* = t_f (g/L_f)^{1/2} (Q^*)^{1/3}$	$t^* = t_{sw} (g/L_{sw})^{1/2} (m_{sw}^*)^{1/3}$
(e)	*Dimensionless density difference, θ**	$\theta_T^* = \beta_T (T - T_0)(Q^*)^{-2/3}$ $\theta_{smoke}^* = \frac{\beta_T Y_{smoke} \Delta H_c}{y_{smoke} c_p (Q^*)^{2/3}}$	$\theta_{sw}^* = \beta_{sw} Y_{salt} (m_{sw}^*)^{-2/3}$

Table 1 Comparison of the dimensionless variables between fire and salt-water plume

2.1.2 Predicting Detector Response Time using Salt-water results

Salt-water modeling has been a useful tool to characterize the dispersion (i.e. temperature and smoke species) in fire induced flows. Coupled with the advanced laser diagnostics, quantitative dimensionless field data obtained from the salt-water model can be useful to predict fire events especially when fire data are lacking.

An application of such approach was to use the dimensionless salt-water quantities to predict the detector response time (t_{ACT}), which consisted of the front arrival time (t_{FA}) and detector lag time (t_{lag}). The dimensional front arrival time (t^*_{FA}) was first determined from the time evolution of the salt-water dispersion, at the instance when the dispersion quantities were seen rising quickly. Using existing Heskestad's detector model[5], the equations were made dimensionless to obtain the dimensionless detector lag time (t^*_{lag}), from which the dimensionless detector response time (t_{ACT}) was found. The dimensionless detector response time was then converted to give the predicted time in the fire configuration.

Heskestad modeled the detection response for the spot-type ionization and photoelectric smoke detector, by defining the smoke entry resistance as a characteristic time constant, τ_d which was particular to the specific detector. The time constant represented the smoke particles transport lag into the detector, which defined the time required for the smoke mass fraction inside the detector, $Y_{smoke,i}$ to be equal to that outside the detector, Y_{smoke}. Heskestad proposed $\tau_d = L_d / u$, where L_d [m] measured the geometric entry resistance (equivalent to chamber-filling time), and the equation was given by

$$\frac{dY_{smoke,i}}{dt} = \frac{Y_{smoke} - Y_{smoke,i}}{L_d/u} \tag{2.13}$$

If the rate of smoke build-up in the sensing chamber and τ_d were constant, and the initial smoke mass fraction in the detector chamber was zero; then the smoke mass fraction outside the detector at the response time, $Y_{smoke,r}$ may be approximately given by

$$Y_{smoke,r} = \left(\frac{dY_{smoke}}{dt}\right) t_{lag} = Y_{smoke,ir} + \frac{L_d}{u}\left(\frac{dY_{smoke}}{dt}\right) \tag{2.14}$$

where $Y_{s,ir}$ was the smoke mass fraction required inside the detector to trigger an alarm, which was also commonly known as its static response threshold. Hence, the detector lag time, t_{lag} after the arrival of the smoke was given by,

$$t_{lag} = \frac{Y_{smoke,ir}}{\left(dY_{smoke}/dt\right)} + L_d/u \tag{2.15}$$

The detector lag time was based on a single characteristic response time of the detector related to the residence or mixing time required for the smoke to reach the activation threshold of the smoke sensor in the detector, which was found to be 1.29 ± 0.51 [%/ft obscuration] and 2.06 [%/ft obscuration] based on the actual ionization detectors and photoelectric detectors used in the full-scale fire tests in ATF respectively. L_d values which is specific to any detector needed to be experimentally determined, and Bj□rkman[34] reported the typical values of L_d for a ionization and photoelectric smoke detector to be 3.2 ± 0.2 m and 5.3 ± 2.7 m respectively and is valid if the detector's local velocity exceeded 0.16 m/s.

The dimensionless detector lag time may be then expressed as,

$$t^*_{lag} = \frac{\theta^*_{smoke,ir}}{\left(d\theta^*_{smoke}/dt^*\right)} + \frac{L_d / L_f}{u^*_f} \tag{2.16}$$

where $\theta^*_{smoke,ir} = Y_{smoke,ir}\left(\Delta h_c\right)\left(y_{smoke} c_p T_o\right)^{-1}\left(Q^*\right)^{-2/3}$ represented corresponding dimensionless smoke mass fraction activation threshold and $d\theta^*_{smoke}/dt$ was the

dimensionless rate of change of the smoke mass fraction outside the sensing chamber, and u_f^* was the dimensionless velocity of the flow outside the sensing chamber. The dimensionless rate of change of the smoke mass fraction and dimensionless velocity thus can be obtained experimentally from the salt-water model, and hence allowing the prediction of the detector lag time.

For gas velocity less than 0.16m/s, another detector model proposed by Clearly[35] which involved the use of dwell time and mixing time may be appropriate, but beyond the scope of this paper.

2.2 ATF High-Bay Full-Scale Compartment Test Matrix

Full scale tests were conducted in a large well-ventilated compartment (4.42m high), opened at both ends and adjoining two partial corridors on one of the side walls at the ATF facility as shown in **Figure 2 (a)**. The ceiling of the compartment consisted of 0.54m tall evenly-spaced (0.71m) beams, forming 19 bays as shown in **Figure 2 (b)**. Miters were cut at the end of the ceiling beams along the side-wall opposite the corridors as shown in **Figure 2 (c)**. The specific dimensions of the beams were found in **Appendix A Figure 31**.

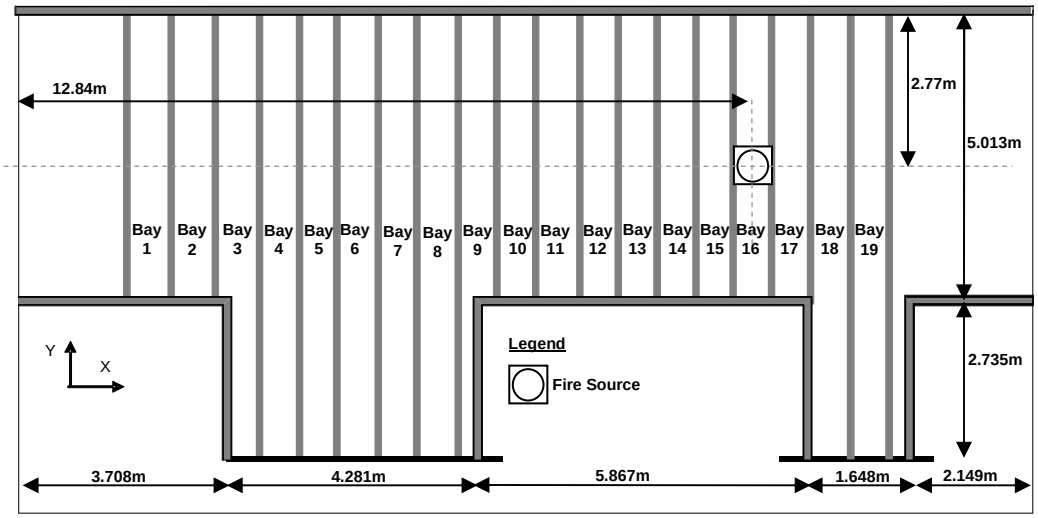

(a) Top-view

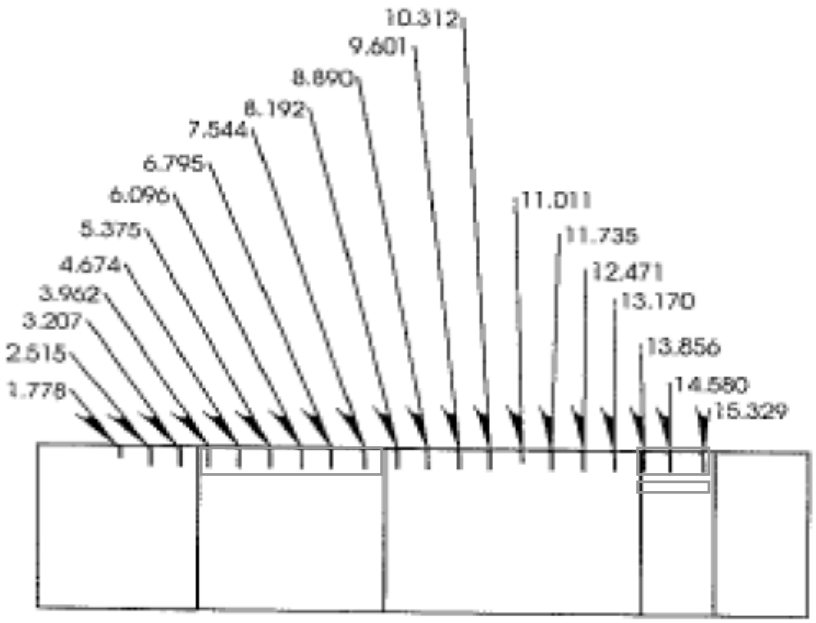

(b) Side-view

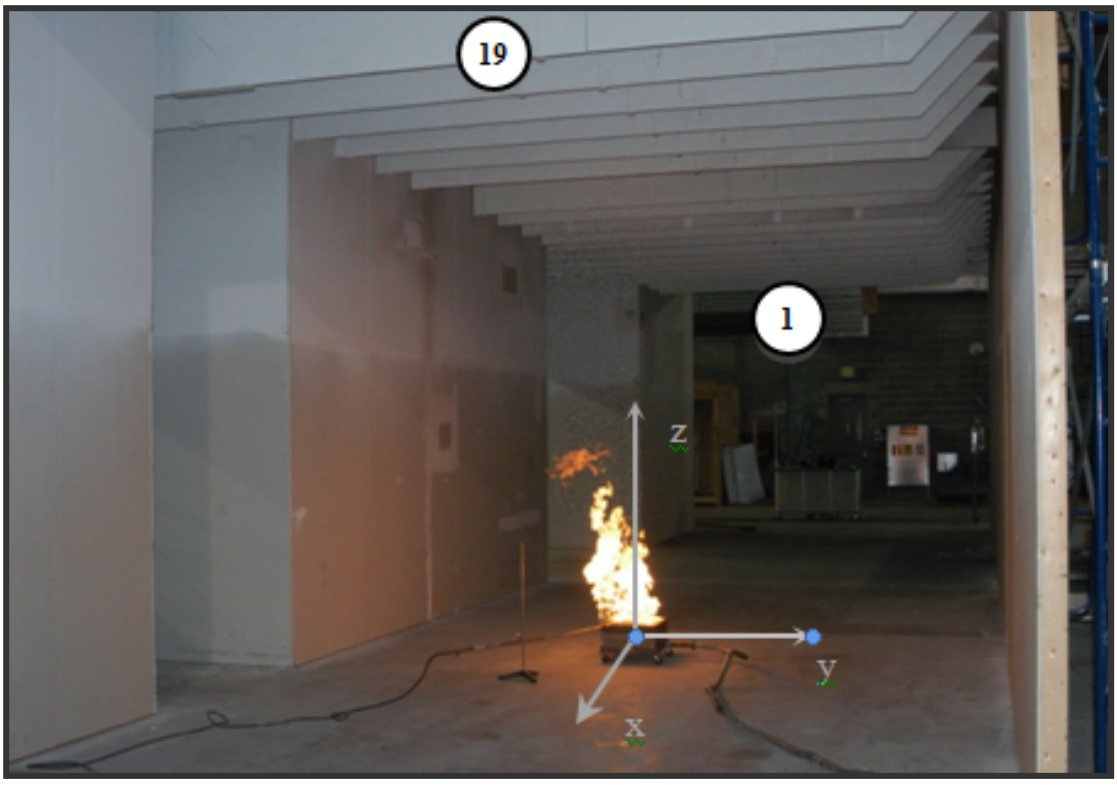

(c) Isometric view

Figure 2 Full-scale Fire Compartment (a) Top-view (b) Side-view (c) Isometric

For each of the bays, it was instrumented with three thermocouples at different beam heights (0.05, 0.15, and 0.46m below the ceiling) along the centre of the ceiling. Additional sixteen thermocouples were placed 0.304m apart along the beams for three of the bays (2, 4, and 10). Selected bays (2, 6, 13, and 19) were each instrumented with a photoelectric smoke detector, two ionization smoke detectors, an optical density meter and a hot wire anemometer. The exact locations of the instrumentation were tabulated in **Appendix B Table 5** and **Table 6**. For all experiments, the source was placed 12.84 m inside the length (17.72m) of the enclosure and about centered (2.77 m) along its span (5.01 m).

A total of 20 experiments which involved different fire source types i.e. natural gas burners, heptane pool fires, pine-wood cribs and polyurethane foams were carried out as shown in **Table 2**. Only the steady sources (Burner fires and pool fires) were analyzed in this research, while future work may address dynamic fire sources.

S/N	Source Type	Total Heat Release Rate [kW]	Q^{*} [a] [$x10^{-3}$]	Remarks
1	Natural Gas Burner [No Ramp]	300	4.51	0.41m square burner, fire at 0.292m above ground
2		250	3.87	
3		150	2.49	
4		75	1.34	
5		50	0.93	
6		25	0.48	
7	Heptane Liquid Pool	346	5.76	Small round pan (D = 0.305m)
8		346	5.76	
9		153	2.63	Medium round pan (D = 0.457m)
10		153	2.63	
11		159	2.72	
12		159	2.72	
13		60	1.03	Large round pan (D = 0.61m)
14		60	1.03	
15-17	Pine Wood Crib	400	-	11 layers, 7 sticks per layer, 1.9cm square pine sticks of 76.2m long
18-20	Polyurethane Foam Blocks	400	-	0.762m x 0.762m x 0.127m high

[a] L_f defined as the characteristic room height of the room from the virtual origin[36], $z_o=1.02-0.083Q^{2/5}$

Table 2 The ATF High-Bay Compartment Test Matrix.

2.3 UMD Salt-water 1/15th Scale Compartment Test Matrix

A series of salt-water experiments using a 1/15th scale clear acrylic model of the ATF compartment were conducted in University of Maryland Fire Protection Engineering Salt-water Laboratory. The saltwater testing facility included a large fresh-water tank where the compartment model was supported within the tank and pre-determined saltwater flows of known salt mass fraction were injected through a specially designed large source injector from a gravity feed system as shown in **Figure 3**.

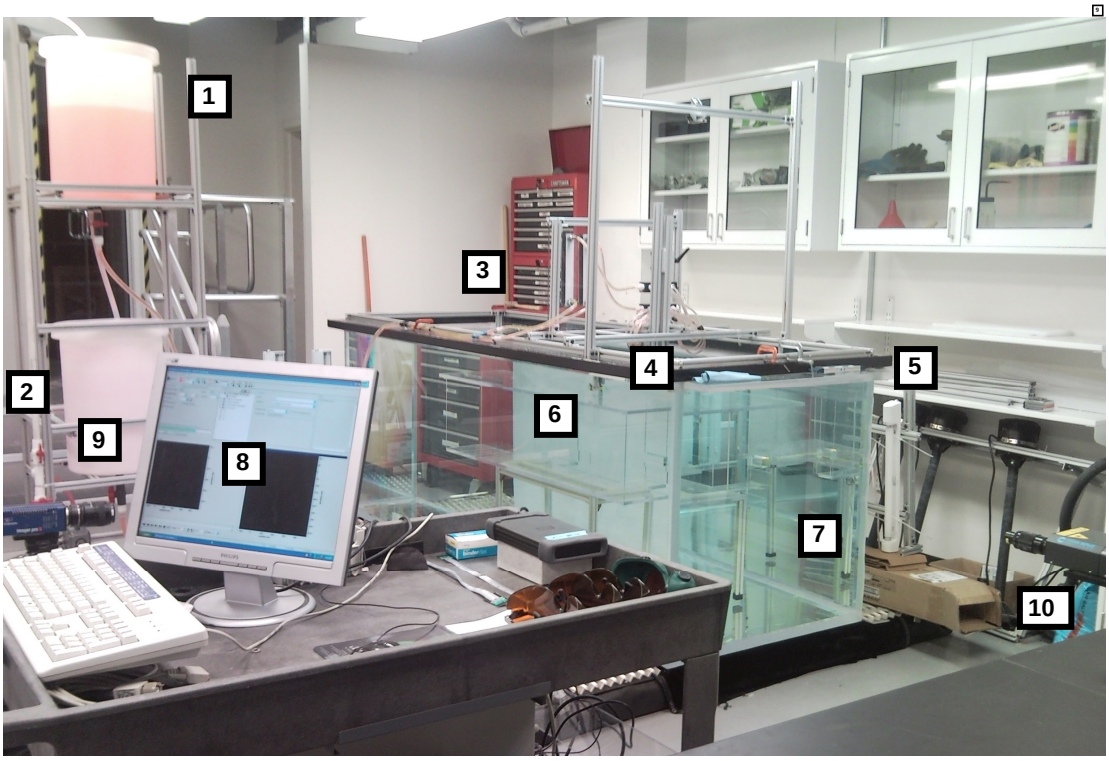

Figure 3 Salt-water Test Facility. (1) Salt-water tanks; (2) Circulating pump; (3) flow meter; (4) Source Injector; (5) Back-lighting; (6) Model (7) fresh water tank; (8) PIV/PLIF Image Acquisition System; (9) Canon/CCD Camera (with filter); and (10) 30mJ double-pulsed green Nd/YAG laser with focusing lens system.

The 1/15th scale model was selected based on the following 3 criteria,

(i) Need to design for turbulent flow within the complex

$$Gr_{source}^{sw} = \frac{\beta_{sw} \dot{m}_{salt} g L_{sw}^2}{\rho_o \upsilon^3} > 10^9$$

(ii) Fit model within the fresh water tank [2.375 x 0.79m x 0.85m high]

$$\frac{L_f}{L_{sw}} > \frac{7.75m}{0.79m} > 10$$

(iii) Limitation of Field of view for PIV [designed to be 600mm]

$$\frac{L_f}{L_{sw}} > \frac{7.75m}{Field\ Of\ View = 0.6m} > 13$$

The saltwater flows were then investigated using various non-intrusive experiment techniques. The blue-dye technique being the simplest approach was used to visualize the flow within the compartment, and to characterize the salt-water setup, the injector flows, and its repeatability. This technique was useful for qualitative analysis of the general flow and helped to identify critical or interest regions for further quantitative analysis. Quantitative measurements of the flow velocity and concentration at a particular interest region were carried out using the Particle Image Velocimetry (PIV) and Planar Laser Induced Fluorescence (PLIF) techniques. It was the interest of the research to focus on the beam ceiling flow at Bay 19 (B19) which was seen from the blue dye experiments to be complicated because the bay was opened into the partial doorway, yet the transverse bay were close to the opened end of the corridor, not forgetting the presence of the miters channeling the flow between the bays and the spilled flow over the beams.

A total of 11 experiments were conducted, four (4) of which were blue dye experiments, five (5) were PIV experiments, and three (3) were PLIF experiments as summarized in **Table 3** at the end of the following sections.

2.3.1 Blue Dye Salt-water Flow Visualization Technique

One and three experiments involving salt-water volumetric flows of 900ml/min and 750 ml/min respectively were carried out respectively. Blue dye powder was added to the source salt-water to facilitate the flow visualization at a concentration of 0.05% dye by weight. The intent of was to ensure that the newly designed large source injector was reliable and the experiments based on same or different salt-water flow rates were reproducible.

Figure 4 Blue Dye Salt-water Experiment

Camera, Canon EOS 40D was used to capture images (3888x2592 pixels) of the salt-water flow at a frequency of 3Hz for a duration of 200s. 50mm lens system were used with the exposure time and F-stop set at 1/125 and f/3.5 respectively. A frame of vertical 18W white-light florescent tubes was installed behind fresh-water tank to provide the necessary back-lighting for better contrast as shown in **Figure 4**.

An orifice-like large source injector connected to 9 small tubes was designed for high volumetric flow to be in range of 500-2000 ml/min so as to simulate large fire source without significantly increased the duration of the salt-water experiment.

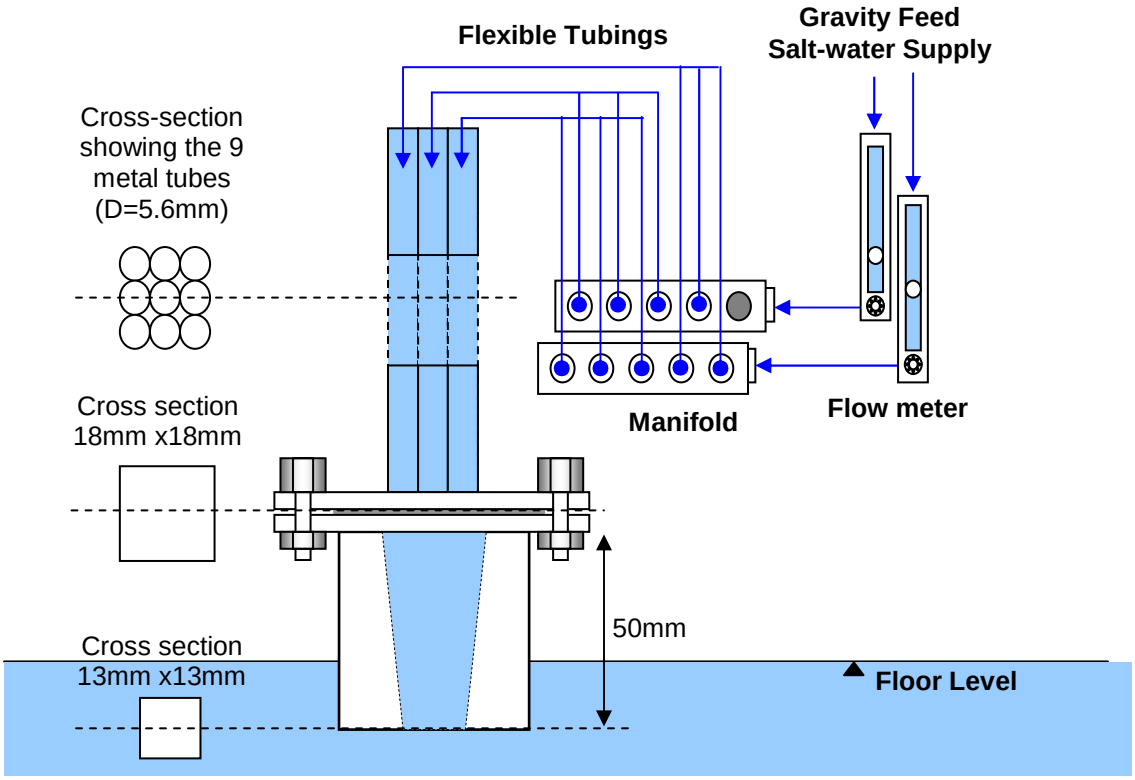

Figure 5 Schematics drawing of the large source injector

The Morton length[37,38,39], L_M was commonly used to determine the flow region in which the buoyancy, B of the flow dominated the original momentum, M of the flow at the source, for which the plume-like behavior were achieved at a streamwise location of $5\times L_M$. For a constant injection velocity, U_{inj} through a square source, L_M was given as

$$L_M = \frac{M^{3/4}}{B^{1/2}} = \frac{\left(U_{inj} L_{inj}\right)^{3/2}}{\left(\frac{\rho_{source} - \rho_0}{\rho_{source}} g U_{inj} L_{inj}^2\right)^{1/2}} \tag{2.17}$$

2.3.2 Particle Image Velocimetry (PIV) Technique

Five (5) PIV experiments were conducted to obtain quantitative measure of the instantaneous flow velocity field across a selected planar area of a salt-water dispersion as tabulated in **Table 3**. The planar areas of interest were at B19; three of the planar views were along the corridor (X-Z plane), one of which was along the beam (Y-Z plane), and one of which was across the bay (X-Y Plane). Two of the X-Z planes were at the centre of the corridor, which one of which was at the detector location offset away from the partial corridor as shown in **Figure 6**.

The La Vision Davis 7.2 PIV system consisted of the image acquisition system of a CCD Camera (4MegaPixels) fitted with high-pass filter to capture the field flow, in which 50μm polyamide seeding particles (0.5% by weight) added to the source tracing the flow field were illuminated by a 30mJ double-pulsed green Nd/YAG laser

(λ=532*nm*). At a frequency of 3 Hz, two images of relatively short laser pulses time separation, *dt* were recorded, after which the paired images were cross-correlated in the post-processing machine to obtain the instantaneous and average flow velocities.

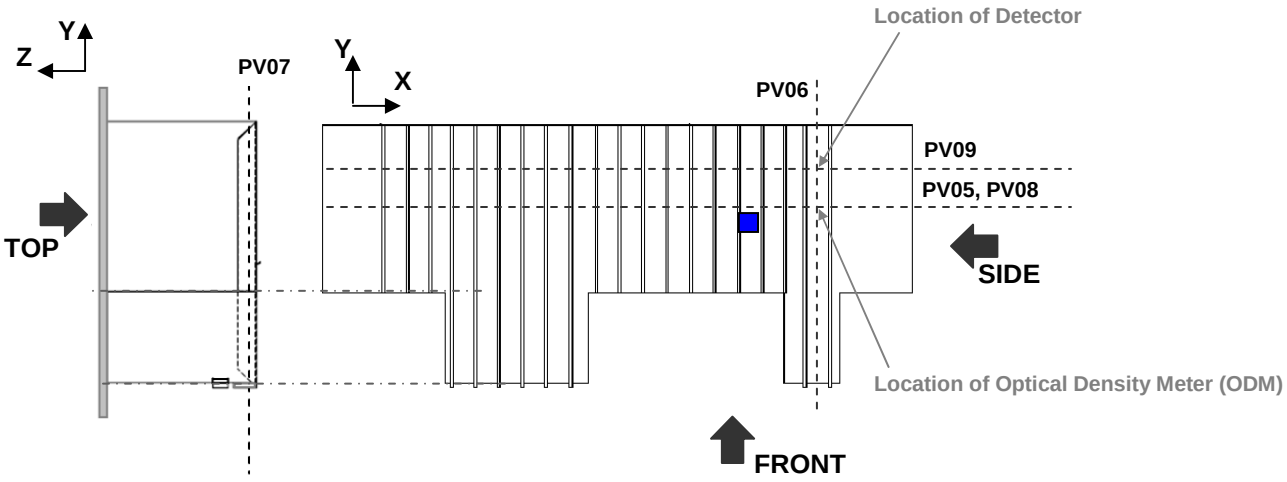

Figure 6 Selected PIV Planar views for velocity measurements

The pulse separation, *dt* was determined in a way that the particles image shift, *ds* is in the interval given by the resolution of the system and maximum allowable particle shift i.e. 0.1pixel < *ds* < ¼ Interrogation Window Size. It was however recommended by the developer for the mean particle image shift to be approximately 5 times the seeding particle image diameter, d_i for a perceptible flow field measurement, whereby

$$d_i = \sqrt{\left(Md_p\right)^2 + \left(d_{diff}\right)^2}\ ; \qquad (2.18)$$

for which

$$M = \frac{Chip\ Size}{Field\ Of\ View}$$

$$d_p = seeding'\ s\ mean\ diameter = 50\,\mu m$$

$$d_{diff} = 2.44 f_{\#}(M+1)\lambda$$

$f_{\#} = f\ number\ of\ the\ lens\ system,$
$\lambda = the\ wavelength\ of\ the\ incident\ light\ on\ the\ particle$

2.3.5 Planar Laser Induced Fluorescence (PLIF) Technique

Three (3) PLIF experiments were conducted to obtain quantitative measurements of the salt-water dispersion concentration, equivalent to scaling quantities for fire's temperature and smoke concentration. One-color PLIF methodology was used whereby known concentration of Rhodamine 6G tracer dye was added to the source tank homogenously, which fluorescenced when the planar laser sheet excited it. A camera lens filter that cut off light wavelength at 540nm was used to eliminate effects of strong reflections of the laser from walls or particles.

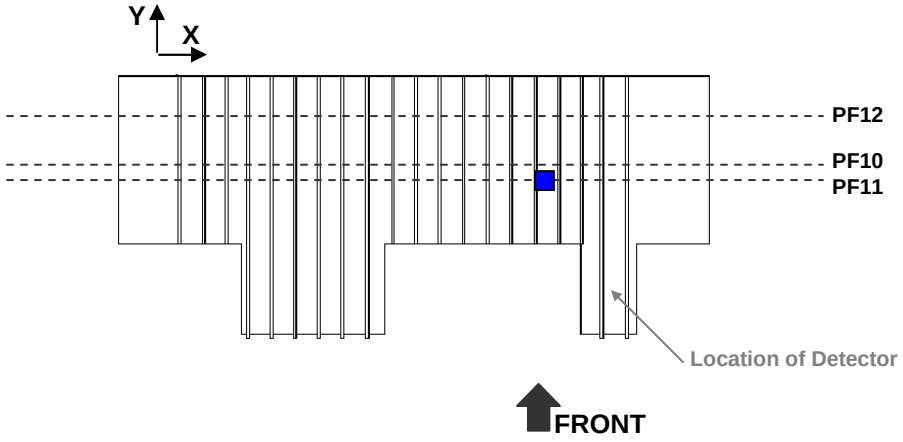

Figure 7 Selected PLIF Planar views for concentration measurements

The laser emission power was set to be below the saturation energy of the tracer dye, yet in the upper fluorescent signal strength to provide a longer laser path in which less than 5% of the signal loss was acceptable. The dye concentrations used for PF10, PF11, PF12 were 0.1mg/l, 0.5mg/l and 0.5mg/l respectively. All the planar laser sheets were along the corridor in the X-Z plane with the images taken from the front but at different y-coordinates as shown in **Figure 7**.

Prior to the conduct of the experiment, a calibration curve matching the known dye concentration and the image intensity was attained. Assuming the concentration of dye and salt diluted similarly, the camera signal (image) intensity, I_{PLIF} was a function of the molecular density in a volume, which was related to the concentration of the dye, [dye] as given by

$$I_{PLIF} = C_1 [dye] = C_1 C_2 [salt] \qquad (2.19)$$

where $[salt] = Y_{salt}(1000+760Y_{salt})$ in kg/m^3

The parameter, C_1 of the calibration curve was determined using different known dye concentrations in the salt-water solution. C_2 related the initial dye concentration to the initial mass salt concentration. C_1 was determined to be 1.36×10^{-4} mg/l per count and C_2 was determined to be 1076mg/kg and 251mg/kg for PF10 and PF11/PF12 respectively. From the above equation (2.18), the local mass salt fraction may be calculated from the experimental measures of the dye fluorescence strength.

Inhomogeneities of the planar laser intensity distribution from the central beam axis will decrease the accuracy of the results if an uniform intensity distribution was assumed. Hence, the laser sheet images were recorded and processed (sheet processing function) prior to the experiment so that the experimental images could be normalized with the averaged sheet image to account for variations within the laser sheet. The background images were also recorded, to be later subtracted from the experimental images.

Images of the fluorescent dye and flow dispersion were recorded at a frequency of 3Hz, for 240 seconds during the experiments. After which, the experimental images were post-processed in a certain manner to eliminate the systematic errors. Background (average) subtraction was applied to the experimental images before the correction to the image intensity (sheet correction function) were done using the average sheet image which contained information on the laser profile. Thereafter, the calibration curve was applied to obtain the dye concentrations.

ID	BD01	BD02-04	PV05	PV06	PV07	PV08	PV09	PF10	PF11	PF12
Diagnostics	Blue Dye	Blue Dye	PIV	PIV	PIV	PIV	PIV	PLIF	PLIF	PLIF
Camera Orientation	Front	Front	Front $_{XZ}$	Side $_{YZ}$	Top $_{XY}$	Front $_{XZ}$	Front $_{XZ}$	Front	Side	Side
Image Size [Pixels^2]	3888 x 2592		2048 x 2048					2048 x 2048		
FOV [mm]	1249	1267	583	587	554	384	373	1275	1293	1243
Lens [mm]	50	50	60	50	28	60	60	60	60	60
F-stop	f/3.5	f/3.5	f/2.8	f/3.5	f/3.5	f/2.8	f/2.8	f/2.8	f/2.8	f/2.8
Camera Exposure [s]	1/125	1/125	1/20000					1/100		
Laser interval, dt [x10^3 μs]	-	-	50	50	50	15	15	-	-	-
Volumetric Flow rate [ml/min]	900	750	750	750	750	750	750	750	750	750
Salt Mass Fraction	0.105	0.105	0.105	0.105	0.105	0.105	0.105	0.10	0.10	0.10
Characteristic Room Height [b], L_{sw} [m]	0.291	0.291	0.291	0.291	0.291	0.291	0.291	0.291	0.291	0.291
Characteristic Velocity, U [mm/s]	0.0356	0.0335	0.0335	0.0335	0.0335	0.0335	0.0335	0.0329	0.0329	0.0329
m^*_{sw} [×10^{-6}]	9.79	8.16	8.16					7.74		
Re_D [×10^4]	5.49	4.57	4.57					4.57		
Gr^{sw}_{source} [x10^{11}]	5.94	4.95	4.95					4.72		
Momentum Flux, M [× 10^{-7} m^4/s^2)	13.31	9.25	9.25					9.25		
Buoyancy Flux, B [× 10^{-6} m^4/s^3]	10.39	8.66	8.66					8.66		
Morton Length, L_M [mm]	3.84	3.20	3.20					3.20		

[(b)] *Virtual origin was found from the graph of centreline salt mass fraction vs plume height to be +3.3mm.*

Table 3 Salt-water Test Matrix

Chapter 3: Results and Analysis

The paper focused on describing the flows at Bay 19 (which represent a complex flow scenario), and comparing the dispersion quantities between the small-scale salt-water experiment and the full-scale fire experiments. Since the salt-water dispersion was negatively buoyant (falling plume), the experiment images shown in this paper were deliberately inverted to relate to the familiar rising fire plume.

The image results from the blue dye experiments were analyzed and time evolution of the dispersion intensity at location Bay 19 were compared among the different experiments as shown in **Figure 8**. Video processing of the still images were carried to visualize the flow dynamics.

The PIV images were post-processed to obtain the velocity and to describe the dispersion characteristics at Bay 19. The steady-state averaged images of the flow were shown in **Figure 9, Figure 10, Figure 11** and **Figure 12**. The computed velocity at Bay 19 was used later for predicting the detector lag time using the Heskestad's detector model.

The PLIF images were also post-processed to obtain the mass salt fraction, Y_{salt} at both Bay 19 ODM and Detector Locations, which was later made dimensionless to represent the salt-water dispersion, θ^*_{sw} as shown in **Figure 15** and **Figure 16**. The temperature and smoke dispersion data from the full-scale fire experiments were also

made dimensionless to be θ^*_T and θ^*_{smoke} respectively. The evolution of the dimensionless dispersion quantities in dimensionless time at Bay 19 were compared and presented in **Figure 22**. The steady state dispersion quantities were plotted in **Figure 23**. The dimensionless front arrival time from both salt-water and fire experiments were extracted from **Figure 22** and plotted in **Figure 24**.

The detectors' lag times and response times were obtained from the fire experiments and analyzed in its dimensionless form. Heskestad's detector model was used to predict the detector lag time using smoke obscuration measurements from the fire data; and also to predict the detector lag time using dispersion quantities from the salt-water data. The dimensionless detector lag times for the two (2) ionization detectors and one (1) photoelectric detector were plotted and compared in **Figure 26** and **Figure 27** respectively. Combining with the front-arrival times in **Figure 24**, the predicted detector responses times using both fire and salt-water data were shown in **Figure 28** and **Figure 29** for the ionization and photoelectric detectors respectively.

3.1 Validation of the source design for salt-water plume

The average grey-scale intensity of a selected rectangular area (10 x 3mm) at the Bay 19 location was extracted from every of the 600 images taken from each blue-dye salt-water experiment. The intensity of the images, measured in grey-scale, represented the time evolution of the blue-dye salt-water dispersion. Higher dispersion intensity was obtained for the blue-dye experiment (BD01) with the larger

flow rate of 900ml/min as compared to the other experiments with smaller flow rate of 750ml/min.

The background intensity was subtracted from the experiment intensity before the grayscale measurement were inverted, and normalized by its maximum inverted grayscale value. The time for the experiment with the larger flow rate was scaled to match that of the other experiments with smaller flow rates such that the adjusted time, $t_{SW,BD02} = \left(m^*_{SW,BD02} / m^*_{SW,BD01}\right)^{-1/3} t_{SW,BD01}$. The time evolution of all the salt-water dispersion, in terms of normalized inverted grayscale, for the 4 blue-dye experiments was plotted in **Figure 8**.

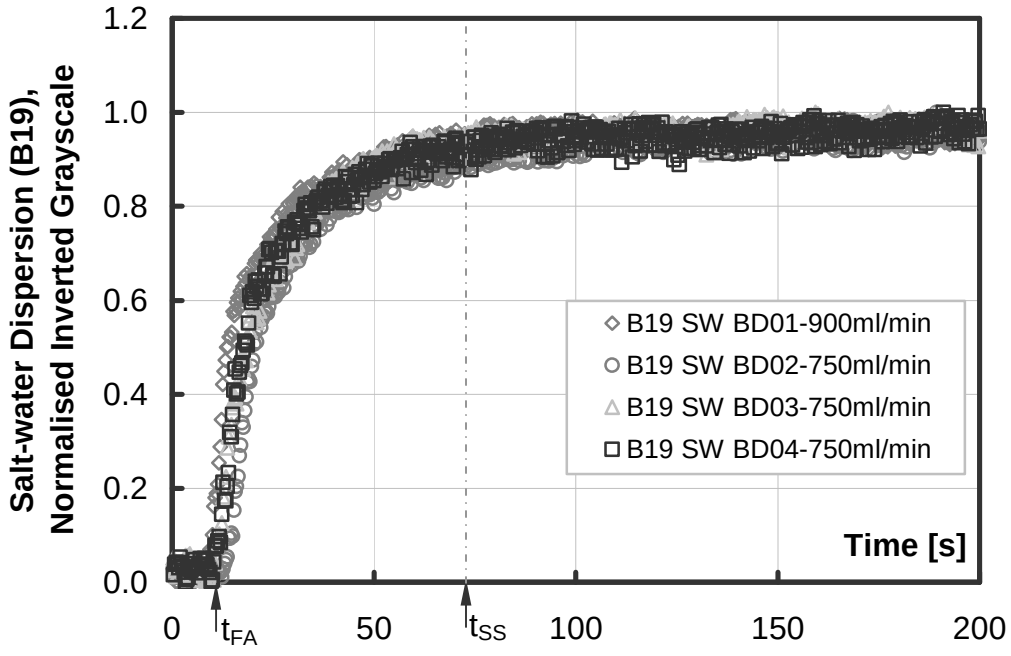

Figure 8 Plot of Salt-water Dispersion at Bay 19 for Blue Dye Experiments

The excellent agreement of the dispersion profiles among the experiments for both different flow rates and same flow rates demonstrated the repeatability of the experiments. The time-evolution profile in **Figure 8** was typical of the plume's temperature or smoke dispersion for a steady heat source, whereby the heat/smoke will arrive at some later time, t_{FA} and its heat/smoke intensity seen increasing before reaching the steady state at t_{SS}, which validated that the newly designed large source injector was suitable for our experiment.

3.2 PIV Results & Images

Cross-correlation of the particles (peak intensity) between two successive images of separation time, dt was performed for each pre-defined sub-regions defined by the interrogation window size and some extent of overlap between the windows as described in **Table 4**. The vector field computed from the initial interrogation window size was then used as a reference velocity field for subsequent decreasing interrogation window sizes, whereby the window shift for the second image were adaptively adjusted using the reference velocity field. This ensured that the same particles were being correlated even if a smaller interrogation window size were defined, thus significantly improved the spatial resolution of the vector field and produced less erroneous vectors.

Thus, the use of 6x6 interrogation window yielded good vector computations despite being smaller than recommended 12x12 interrogation size for the larger field of view.

PV09 was post-processed with a larger interrogation size with less vectors and good spatial resolution was still achieved.

PIV Test	PV05	PV06	PV07	PV08	PV09
Orientation	Front $_{XZ}$	Side $_{YZ}$	Top $_{XY}$	Front $_{XZ}$	Front $_{XZ}$
Field of View	583	587	554	384	373
Chip Size [mm]	15.2	15.2	15.2	15.2	15.2
Magnification, M	0.0260	0.0258	0.0274	0.0395	0.0406
Image size [pixel]	2048	2048	2048	2048	2048
Scaling factor [mm/pixel]	0.285	0.287	0.2705	0.188	0.182
Particle image diameter, d_i [x10^{-6} m]	3.95	4.84	4.86	4.26	4.29
Ratio of d_i : chip's pixel size	0.53	0.65	0.66	0.58	0.58
Est. Particle Velocity [mm/s]	15	15	15	15	15
Laser interval, dt [x10^3 μs]	50	50	50	15	15
Est. Particle shift, ds [pixel]	2.63	2.62	2.77	1.20	1.24
Laser thickness [pixel]	5.27	5.23	5.55	8.00	8.24
1st passes [pixel] (Overlap)	64 (50%)	128 (50%)	128 (50%)	32 (50%)	32 (50%)
2nd passes [pixel] (Overlap)	6 (25%)	6 (25%)	6 (25%)	6 (25%)	12 (50%)
Number of vectors (2nd passes) [x10^5]	1.16	2.62	2.62	2.62	1.16
Maximum B19 V_x[1] [mm/s]	-	-	-13	-	-13
Maximum B19 V_y[1] [mm/s]	-	8	8	-	-
Maximum B19 V_z[1] [mm/s]	-	-4	-	-	-4

[1] Measurement at the Detector location

Table 4 PIV Post-processing Parameters

The laser separation time, dt needed to be optimized. While increasing the laser separation time to produce a larger particle shift may help to increase the accuracy determining the velocity, excessive dt may cause the particles to move out of the laser plane (~1.5mm thick) or exceed the interrogation window size increasing the measurement noise. Based on the initial estimation and the experimental

measurement of the particle shift at B19 detector location, it was concluded that the selection of dt was appropriate.

Figure 9 showed the steady-state averaged images of the salt-water dispersion from Bay 13 to Bay 19. The steady-state entrainment of the ambient fresh water into the salt-water plume was from one direction, following the dominant flow in the positive x-direction, and hence the plume was not symmetrical and slanted to the right towards the opened end of the corridor. It was, however observed that the initial entrainment of the fresh water was from both directions towards the plume.

The ceiling jet flow was changed due to the ceiling obstructions. There was a distinct layered flow over the beams, with clockwise circulating flows within the bays (i.e. in Bay 13 and beyond) of dimensionless distance of 0.5 away from the plume. Interestingly, a boundary layer was developed between 2 opposing flows below the bays to the left of the plume. However, there was no distinct flow within Bay adjacent to the plume (i.e. Bay 14, 15, 19) which could be due to the highly turbulent flow at these bay locations near to the plume.

At the region without the beams (i.e. after Bay 19), the flow of the ceiling jet was close to the flat ceiling, with its depth approximately 10% of the room height. The ceiling jet thickness over the bays was thinner, approximately 7% below the beam, due to the circulating flows within the bays as well as exiting flow from Bay 19 in the negative y-direction.

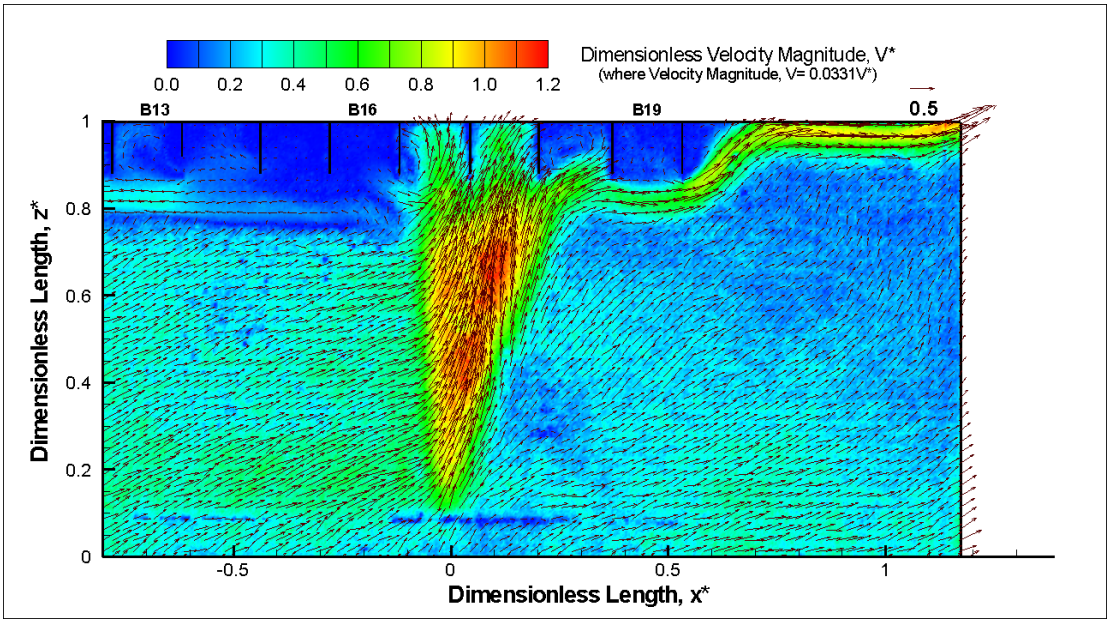

Figure 9 Computed Velocity of the Flow along the Corridor at ODM location (PV05)

Figure 10 magnified the steady-state averaged images of the salt-water dispersion from centre of the plume to end of the corridor using a smaller field of view. It showed similar flow structures as described above, with the ceiling jet flow below the beam, and no distinct flow within Bay 18, or 19. It was noted that the velocity of the ceiling jet was lower below the bays than at below the ceiling after the bays. A higher maximum centerline plume velocity was obtained since a larger field of view with shorter dt reduced the chances of flow being out of the laser's plane for the flow of higher velocities.

Figure 11 showed the steady-state averaged images of the salt-water dispersion from centre of the plume to end of the corridor at the detector locations which was closer to the miter's end. Since the plume expanded radially, the flow entered the plane at B18, and low V_x velocity of the plume was seen at B17. The circulating flow in Bay 18 and Bay 19 became apparent as it was away from the centre of the plume. There was

also a secondary flow developed around the miter from Bay 18 to Bay 19 as shown also in **Figure 12**.

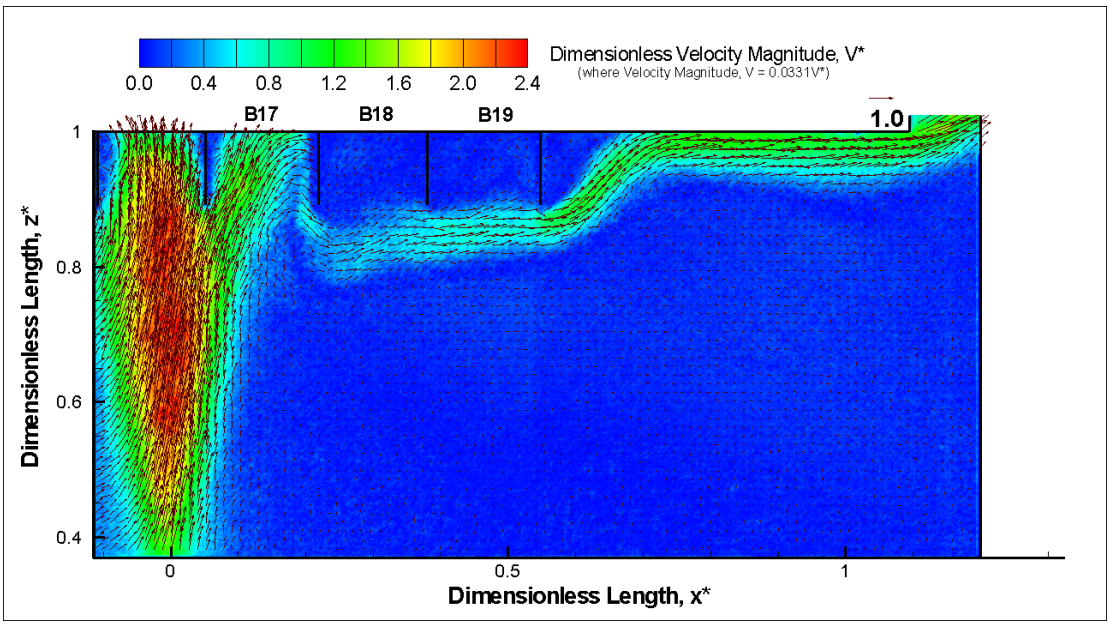

Figure 10 Computed Velocity of the flow at Bay 19 (PV08 – larger field of view)

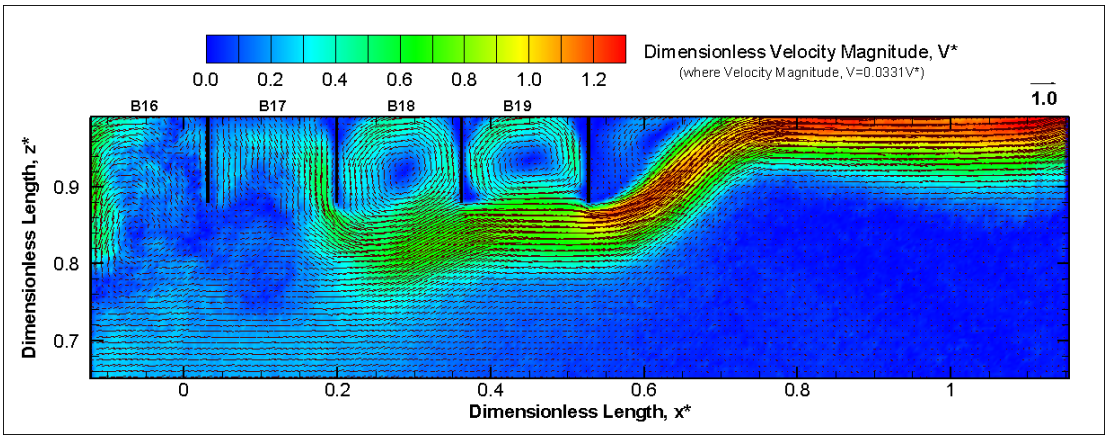

Figure 11 Computed Velocity of the Flow along the Corridor at B19 Detector location (PV09)

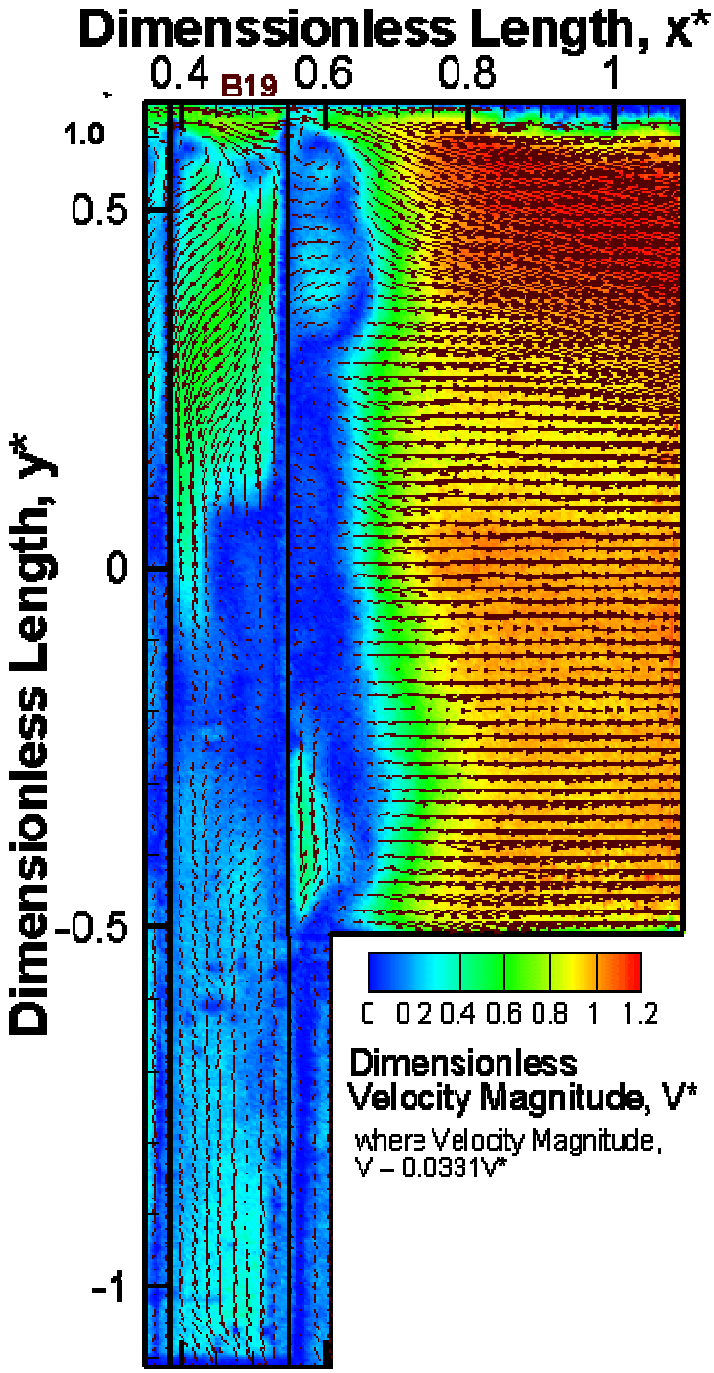

Figure 12 Computed velocity of the flow at Bay 19 (PV07 – Top View)

The flow within Bay 19 was not continuous at the plane of interest that was near to the ceiling. The flow entered B19 across the miter region and a spiral flow was

developed at the detector location. As the flow continued, the interference from the plume caused the flow to be highly mixed and turbulence at the centerline location. After the centerline location, some residual flow was seen exiting out of the Bay 19 in the negative y-direction.

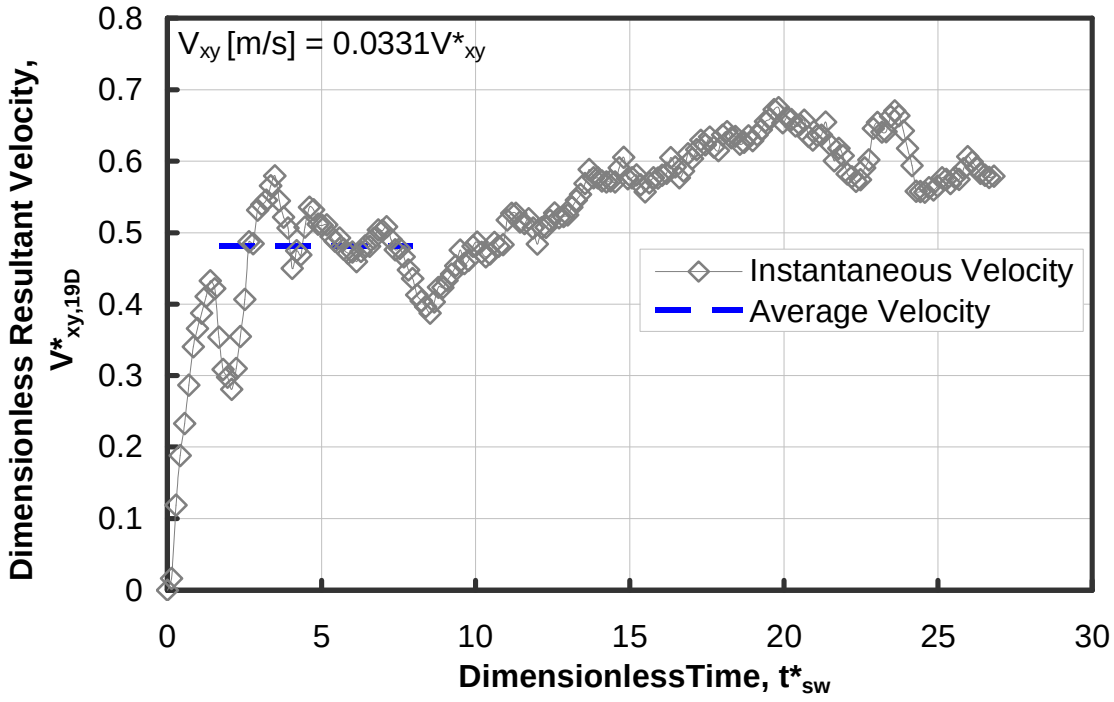

Figure 13 Plot of Dimensionless Resultant Velocity at B19 Detector Location

The time evolution of the resultant velocity of the flow at the detector location was extracted from a selected rectangular area of width comparable to the detector's diameter and shown in **Figure 13**. The average dimensionless resultant velocity was computed from the time of front arrival to the time to steady state, and $V^*_{xy,19D}$ was found to be 0.456. This resultant velocity was used later for predicting the detector lag time.

3.3 PLIF Results & Images

The post-processing procedures of the experiment's images can be summarized in **Figure 14**.

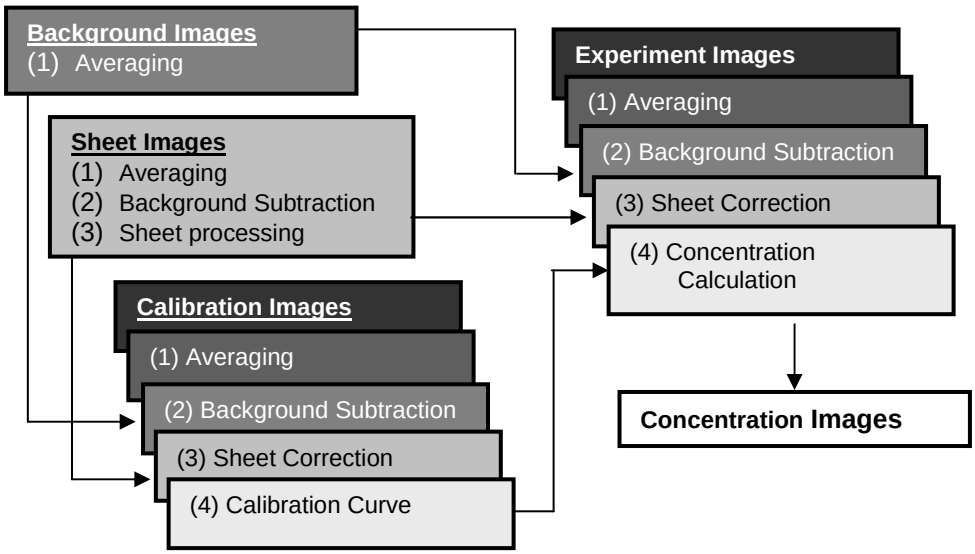

Figure 14 Workflow of PLIF Post-processing

The sheet processing function allowed for smoothing of the sheet images and to reject noise on the laser sheet. An intensity threshold may be applied, below which regions of low intensity were rejected.

It was important to ensure that the calibration of the dye concentration to the imaging intensity was done as closed to the experimental setup as possible. In the experiment where the compartment was not enclosed, calibrating the dye concentration using the model was not possible. Instead, a smaller enclosed tank was used where the tank was filled with 5 different uniform dye concentration of 0.004mg/l to 0.02mg/l with an

interval of 0.004mg/l using the same laser power as that of the subsequent experiments. Depending on the dye concentration, the image intensity along the axis of incident light would appear to be constant for some distance before it started to drop. The distance was known as the critical path length for which beyond it the dye no longer responded linearly with the incident light.

The region of constant image intensity before the critical path length was used for the calibration. A low concentration of dye was chosen because a lower intensity after fresh water was entrained into the plume. An initial dye concentration of 0.1mg/l and 0.5mg/l was added for the source. Yao[20] recommended the use of dye concentration less than 1.5 mg/l to prevent over-saturation of the initial dye.

The normalization of the image in accordance to the peak intensity in the sheet profile will affect the how the calibration of the dye concentration was carried out. The sheet profile used to the normalized the calibration images should be similar to the sheet images used for experimental images in order to avoid systematic errors.

From the concentration images, the salt mass fraction, Y_{salt} can be computed from local salt concentration [SALT], and after which the dimensionless salt-water dispersion, θ_{sw}^{*} was obtained using equation (e) in §2.1.1 **Table 1**.

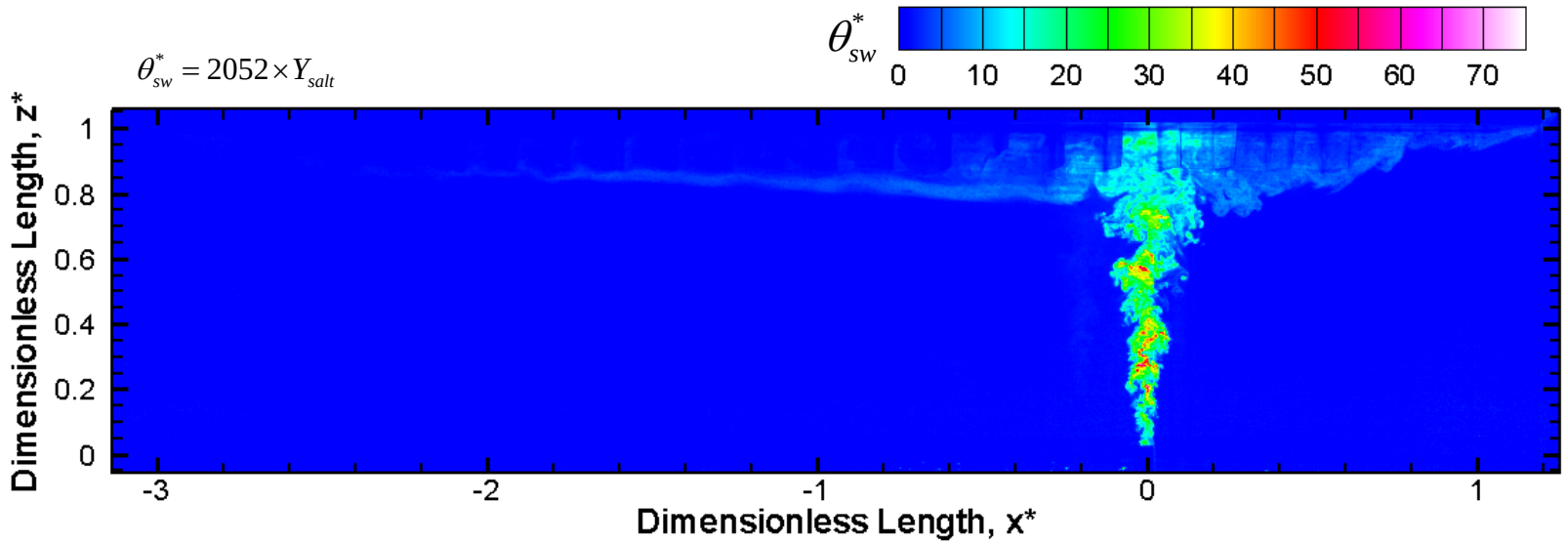

Figure 15 Steady State of PLIF Image of initial concentration of 0.5mg/l ($t^*_{sw} = 26.7$)

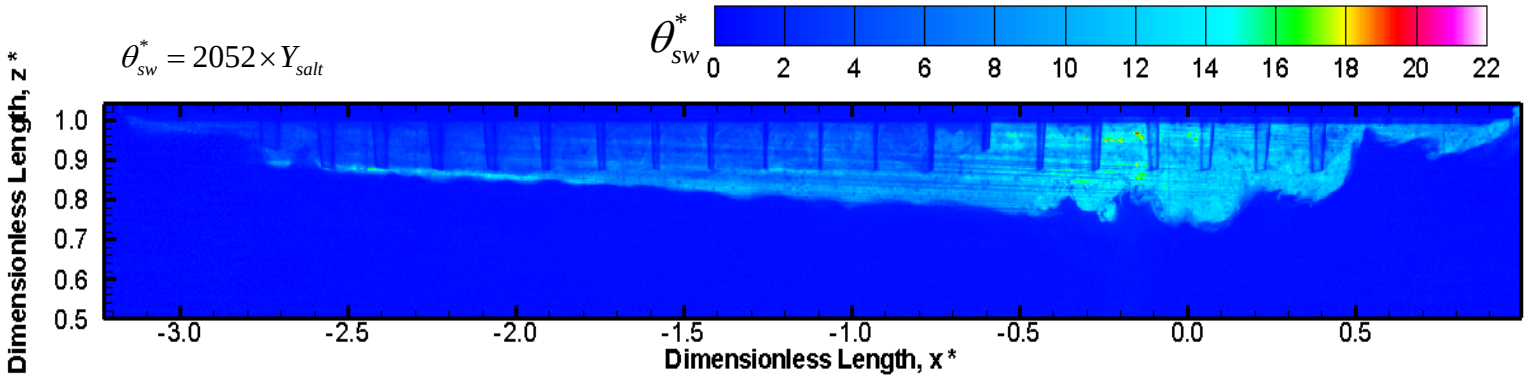

Figure 16 Steady State PLIF of initial concentration of 0.5mg/l, detector location ($t^*_{sw} = 26.7$)

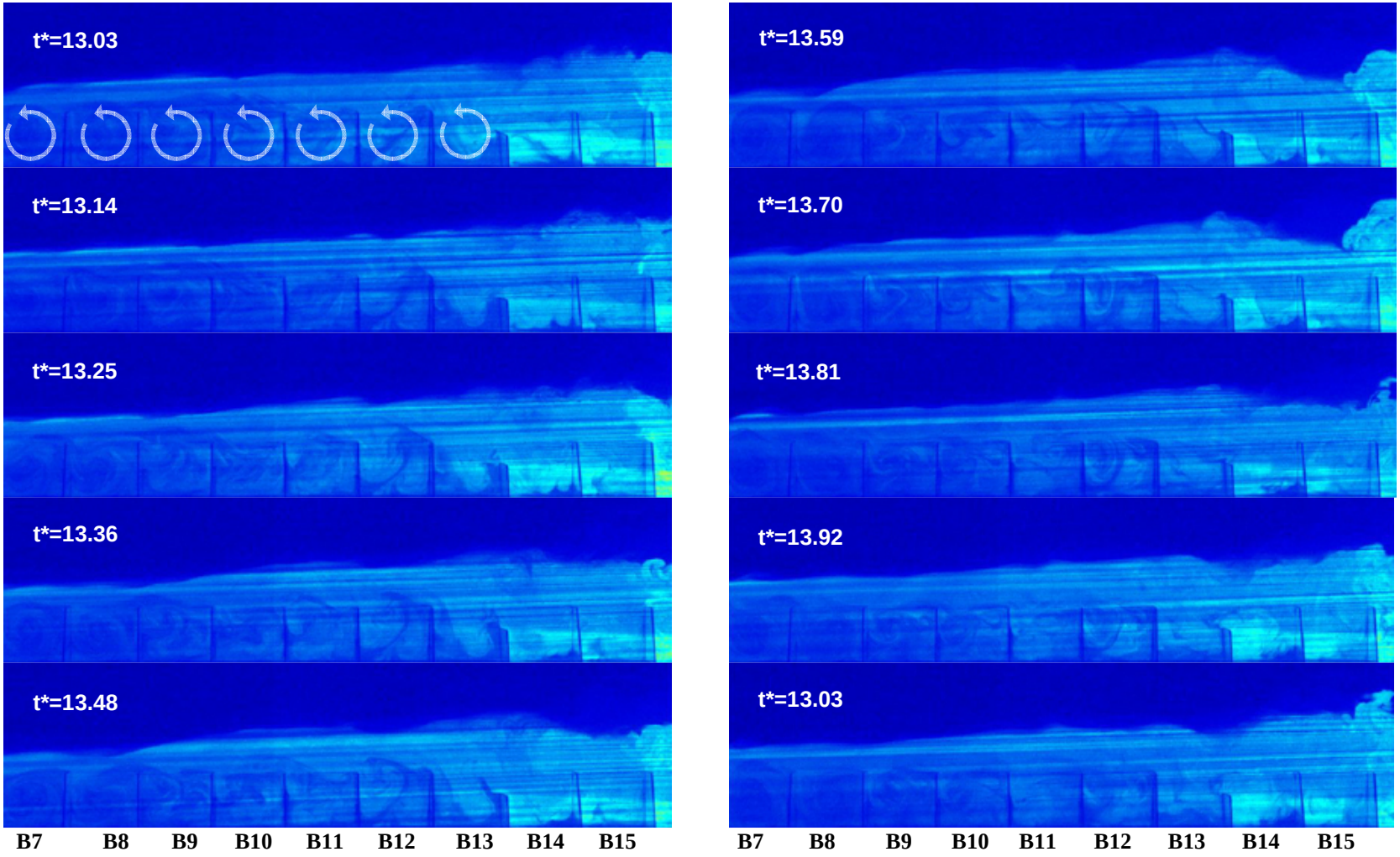

Figure 17 Instantaneous PLIF Images showing the Flow Circulations within the bays (7-13)

The steady state dimensionless dispersion of the salt-water at t^*_{SW} = 26.7 for the experiment PF11 (initial dye concentration of 0.5mg/l) was shown in **Figure 15**. A layer of ceiling jet was also observed below the beam and also close to the flat ceiling region, with the depth of the ceiling jet being approximately 7% and 10% respectively. The weak fluorescent signals after Bay 13 suggested that either the dispersion quantities were very small, or that the laser light were significantly absorbed by the dye ahead of the these regions.

Figure 16 showed the steady state dimensionless dispersion of the salt-water at t^*_{SW} = 26.7 for the experiment PV12 where the laser plane was at the detector location. Since the plume was not present at this plane, the incident light was not absorbed upstream and hence concentration measurement was possible for all the bays. Similarly, a ceiling jet was found below the beams and the circulating flows within the bays were distinctive. At the plane of the detector location, the counter-clockwise circulating flows were clearly seen as shown in the 10 sequential instantaneous images of 1s interval in **Figure 17**.

However, the lower concentration of the salt-water dispersion quantities within the bays as compared to that of the ceiling jet flow suggested lower thermal or smoke concentrations in the fire experiments. This slower buildup of the smoke concentration necessary for detector activation will impact on the detector's response when placed within the bays.

The dimensionless salt-water dispersion at Bay 19 was extracted from every image of the salt-water experiments, as plotted in **Figure 18**.

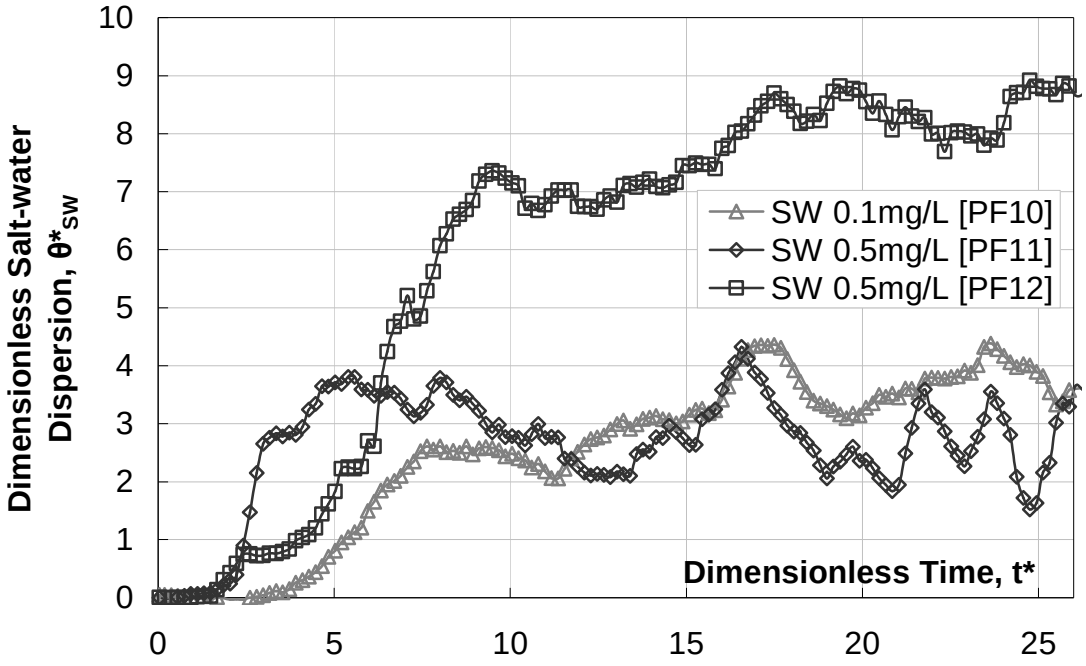

Figure 18 Time Evolution of Salt-water Dispersions

3.4 Scaling Comparison between the Salt-water and Fire Experiments

In order to compare the results from the salt-water experiments with that from the full-scale fire experiments, both the salt-water and fire dispersion quantities, θ*, including flow time and physical space needed to be made dimensionless through the scaling relationships found in §2.1.1 **Table 1**.

When comparing the results, it should be noted that the salt-water analogue presented the adiabatic fire with constant source strength and heat loss effects was not accounted for. The pool fires though had a very different initial heat release rate and burn-out rate; it was found to be reasonable to assume an average heat release rate representative of a steady fire as discussed in later sections. The dimensionless source strength, Q* were tabulated in §2.2 **Table 2**.

3.4.1 Obtaining the dimensionless Fire Dispersion Quantities

The thermal dispersion signature, θ^*_T from a steady fire source resulting in density deficit causing the flow of the gases was scaled by its fire power as given by $\theta_T^* = \beta_T (T - T_0)(Q^*)^{-2/3}$. The temperature measurements at Bay 19 for the first thermocouple at 50mm from the ceiling were made dimensionless and shown in Figure 19 and Figure 20 for the burner and pool fires respectively.

A no-ramp constant heat release rate was used for the burner's fires, while the peak 300 seconds average heat release rate was assumed for the pool fires. Only convective heats were considered for computing the fire power since it was the driving force for the fire-induced flow based on Froude modeling. The radiation factor, Xr was estimated based on the ratio of its convective heat of combustion to total heat of combustion, being 0.67 and 0.86 for the heptane and methane respectively.

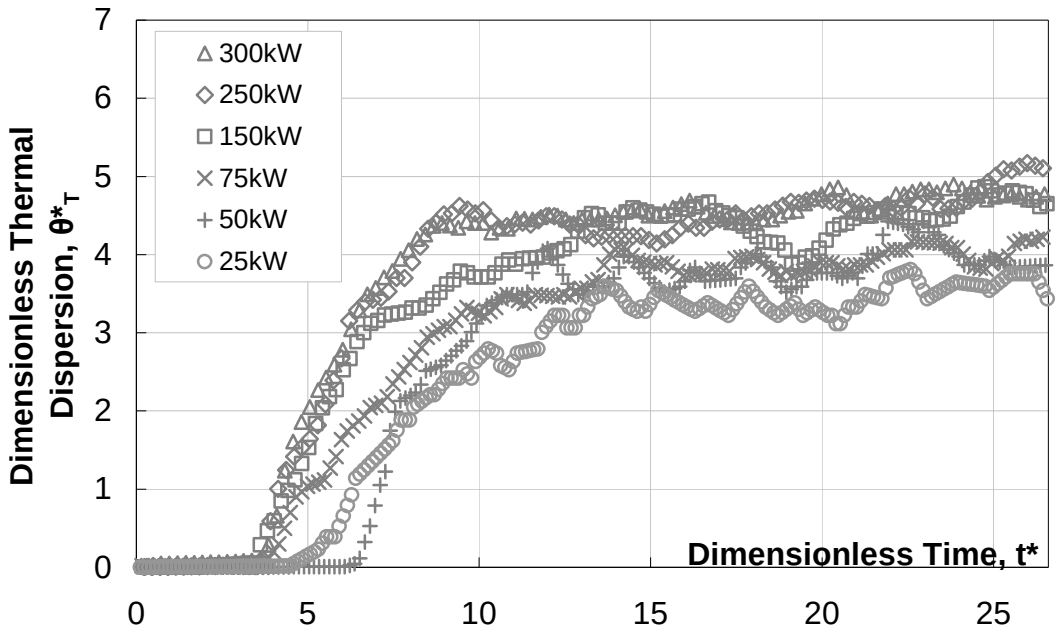

Figure 19 Dimensionless Thermal Dispersion for the Burner Fires

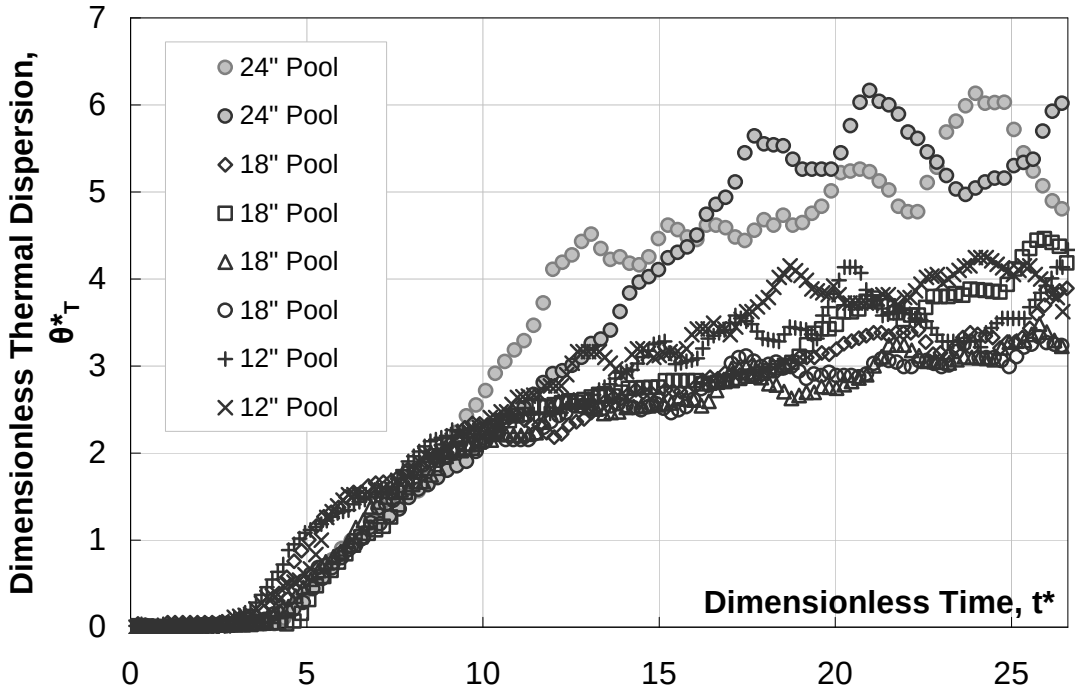

Figure 20 Dimensionless Thermal Dispersion for the Pool fires

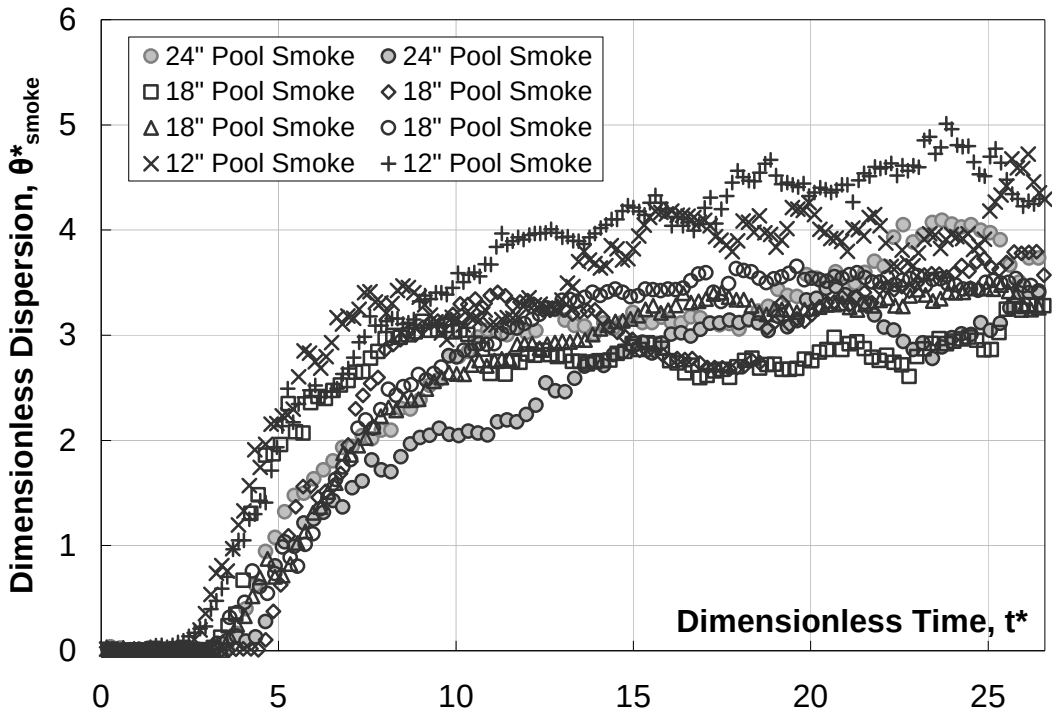

Figure 21 Dimensionless Smoke Dispersion for the Pool fires

The smoke dispersion signature, θ^*_T at B19 was computed for only the pool fires because the smoke yield for the burner fires was low, and did not trigger any smoke detection, as given by $\theta^*_{smoke} = \frac{\beta_T Y_{smoke} \Delta H_c}{y_{smoke} c_p \left(Q^*\right)^{2/3}}$. The heat of combustion, ΔH_c and the smoke yield, y_{smoke} were 27.6 kJ/g and 0.037g/g respectively as given by Tewarson[40] in the SFPE Handbook.

The smoke density of the gases was measured in terms of its extinction coefficient, K using a optical density meter (ODM) whose path length was 1 m. The specific

extinction coefficient, K_m for heptane as suggested by Mullholland[41] was 7.5 ± 0.5 from which the smoke concentration, [smoke] was determined. The mass fraction of the smoke may hence be determined using the smoke concentration as given by

$$Y_{smoke} = \frac{m_{smoke}/V_{mixture}}{m_{mixture}/V_{mixture}} \approx \frac{m_{smoke}/V_{smoke}}{\rho_{mixture}} = \frac{[smoke]}{\rho_{mixture}} = \frac{k/k_m}{\rho_{mixture}} \qquad (3.1)$$

if we assume the volume of the air mixture to be approximately the volume of the smoke.

The dimensionless time evolution of the dimensionless smoke dispersion signature, θ^*_{smoke} shown in **Figure 21**, also showed good agreement among the different heptane pool fires

3.4.2 Comparison of Scaling Results

The scaling theory predicted that the flow time and the dispersion quantities for both salt-water and fire experiments would match if the scaling was done right, such that $t_f^* = t_{sw}^*$, and $\theta_T^* = \theta_{smoke}^* = \theta_{sw}^*$. The time evolution of the dimensionless dispersion quantities for both the fire experiment and the salt-water experiments were shown in **Figure 22**.

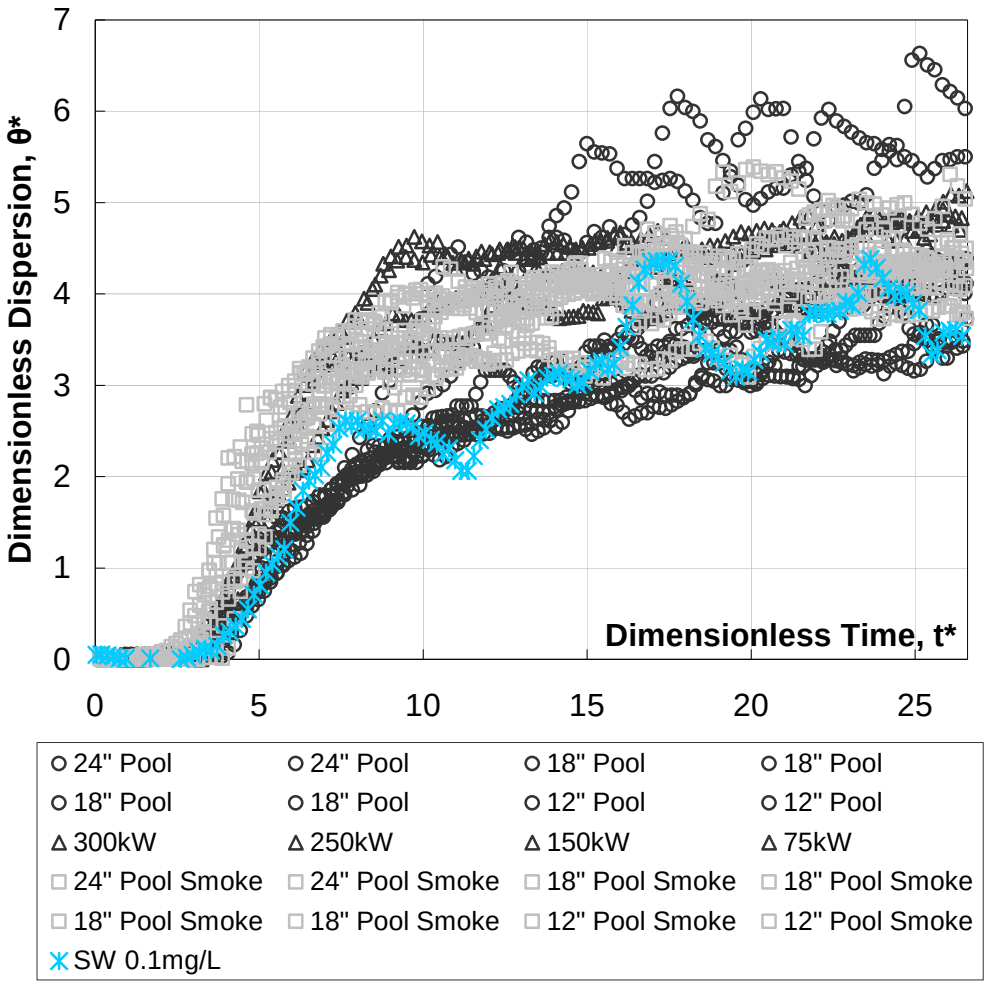

Figure 22 Time Evolution of the Dimensionless Dispersion Quantities for both Full-scale Fire Experiments and Salt-water Experiments.

Both the steady-state dispersion of the salt-water experiments showed good agreement with that of the fire experiments after t*=10. The salt-water experiment with a higher dye concentration (PF11) seemed to reach the steady-state earlier and at a much higher steady state value as compared to the other salt-water experiment, though its signature having a higher fluctuation before stabilizing at later times. The

salt-water with the lower dye concentration corresponded to the lower boundary of the fire experiments, though its signature was less fluctuating.

All experiments showed that the steady state dispersion was attained when t*= 9 with the exception for the salt-water experiment PF11 as shown in **Figure 22**. The time-averaged steady state dispersion quantities for Bay 19 were shown in **Figure 23**, and the dimensionless dispersion, θ* = 4. The high thermal dispersion value for the 24" large pool fires were disregarded for concerns of its radiative feedback as discussed earlier.

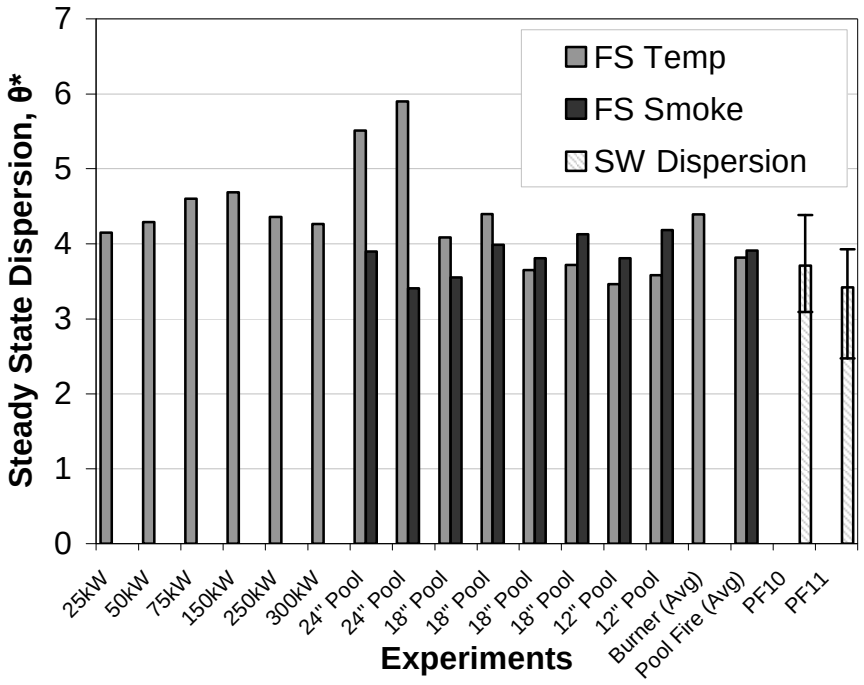

Figure 23 Steady State Dispersion Quantities at Bay 19

3.5 Front Arrival Time, t^*_{FA}

The arrival of the dispersion front for a particular location was determined based on the time where an initial surge in its dispersion was detected. For the fire experiment, both the thermal and smoke time-profiles were used for determining the front arrival at the Bay 19 location. The fluorescence time-profile (i.e. salt mass fraction) of the salt-water experiments were used to determine the front arrival time.

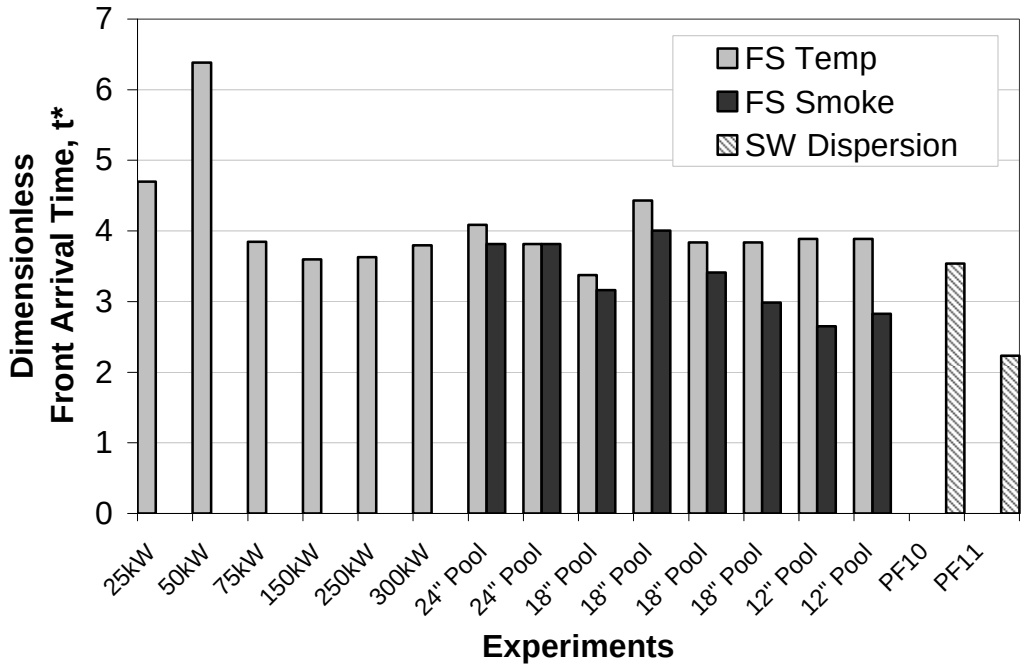

Figure 24 Dimensionless Front Arrival Time

These front arrival times for the fire experiments and salt-water experiments were extracted from **Figure 22**, and the results plotted in **Figure 24**. The dimensionless front arrival times showed good agreement among the different experiments, except for the 50kW burner test. The average front arrival times for the burner fires, pool

fires (thermal), pool fires (smoke) and saltwater experiment (PF10) were 3.68, 3.47, 2.98 and 3.54 respectively.

3.6 Dimensionless Detector Lag Time, t^*_{lag}

Two (2) ionization detectors and one (1) photoelectric detectors were located in each of the 4 bays (Bay 2, 6, 13, 19), and the time of detector activation were recorded for the all the pool fires experiments. The detector activation time, t^*_{ACT} was defined as the sum of the front arrival time, t^*_{FA} and the detector lag time, $t^*_{lag.}$ Hence, based on the actual detector activation times recorded in the experiment, and the front arrival times found in §3.5, the actual detector lag times may be computed and as tabulated in its dimensionless form in **Appendix C Table 7**, **Table 8** and **Table 9**.

As discussed in §2.1.2, Heskestad's detector model in its dimensionless form could be used to predict the dimensionless detector lag time if the detector's local velocity exceeded 0.16 m/s, as shown the **Figure 25**.

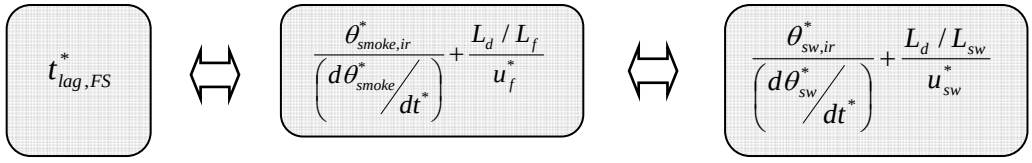

Figure 25 Prediction of t^*_{lag} using Fire and Salt-water data

The average velocity within the vicinity of the detector was 0.45 ± 0.09 m/s based on the dimensionless results from the salt-water experiments at location B19. The initial average rate of change of the dimensionless smoke dispersion, θ^*_{smoke} after its front arrival was calculated from **Figure 21** for all the pool fires. The assumption was reasonable because the detector activation times measured from the fire experiment happened before the steady-state condition was attained. This would also be applicable to real-life scenarios since the design intent of the detection was to alert the occupants of the fire in its incipient stage before it became untenable. Similarly, the dimensionless salt-water dispersion, θ^*_{sw} was obtained from the salt-water experiments from **Figure 18** where slope from PF12 at the detector location were used.

The activation thresholds of the smoke sensor in the detectors, were 1.29 ± 0.51 [%/ft obscuration] and 2.06 [%/ft obscuration] for the ionization detectors and photoelectric detector respectively, based on the information given in the manufacturer's catalogue. Typical values of detector characteristic length, L_d reported by Bj□rkman[34] were 3.2 ± 0.2 m and 5.3 ± 2.7 m for the ionization and photoelectric smoke detector respectively. The optical path length of the optical density meter, L_{ODM} was 0.999998m.

The activation threshold of the detectors were made dimensionless where $\theta^*_{smoke,ir} = Y_{smoke,ir}(\Delta h_c)(y_{smoke} c_p T_o)^{-1}(Q^*)^{-2/3}$. The corresponding dimensionless smoke mass fraction, $Y_{smoke,ir}$ was obtained from its smoke concentration at the activation

threshold obscuration as given by the following equation,

$$1-\frac{[\%/m\,Obscuration]}{100}=\frac{1}{L_{ODM}}\exp\left(-k_m[smoke]\right) \qquad (3.2)$$

The characteristic lengths of the detector were normalized by the length scale of the experiment (i.e. height of the compartment L_f or L_{sw}) in order to made the equation dimensionless. $\theta^*_{sw,\,ir}$ used in the salt-water prediction was assumed to be equivalent to $\theta^*_{smoke,\,ir}$.

The detector lag times were calculated using both fire and salt-water experiment data, and were compared as shown in **Figure 26** and **Figure 27** for the ionization detectors and the photoelectric detectors respectively.

The lag times for the pool fires increased with decreasing pool fires size. The activation threshold of the detector being a constant detector's characteristic would be larger in the dimensionless fields through Froude scaling, hence a longer detector lag time. The prediction of the lag times using fire data was higher than that of the salt-water modeling, because of the different measurement locations used to determine the dispersion slope, $d\theta^*/dt^*$. The slope was determined at the ODM location for the fire experiment while at the detector location for the salt-water experiment, which the latter should be more representative of the detector model if this prediction theory worked.

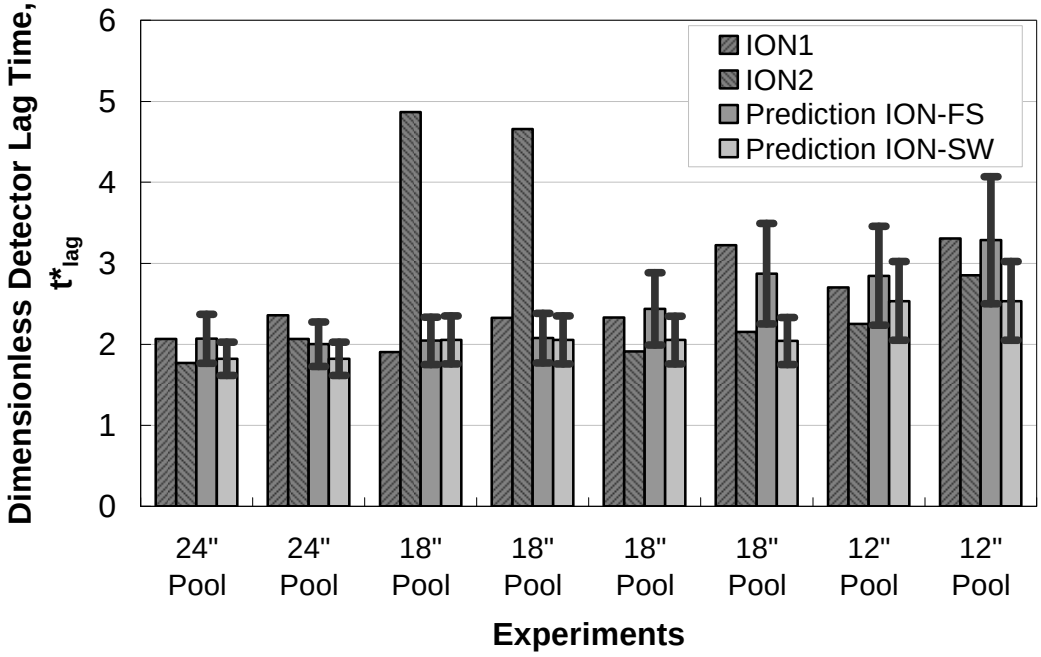

Figure 26 Dimensionless Detector Lag Times for Ionization Detectors

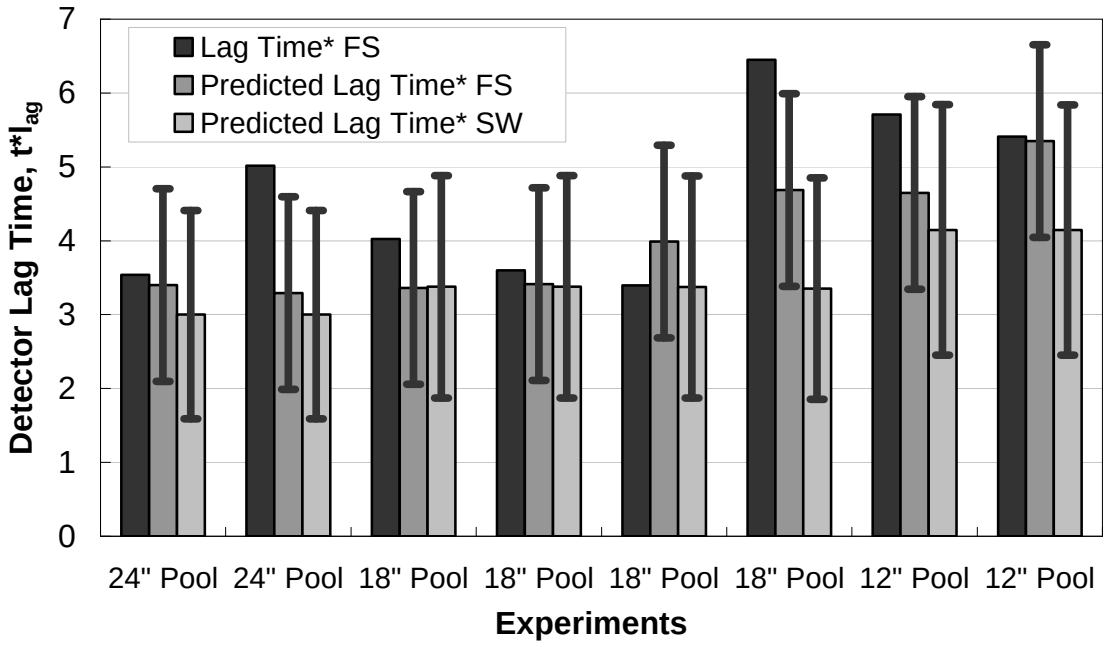

Figure 27 Dimensionless Detector Lag Times for Photoelectric Detectors

Both the predicted lag times using the fire or salt-water data gave excellent predictions of the detector lag times, with exception of two (2) ionization detectors from the 18" pool fires, which could be mal-functioning after many of the previous pool fire tests.

3.7 Dimensionless Detector Activation Times, t^*_{ACT}

The detector activation times were calculated by adding the front arrival times and the detector lag times. While there were few combinations of the front arrival times (based on thermal or smoke signatures) with the different detectors, **Figure 28** and **Figure 29** showed only the activation times for ionization and the photoelectric detectors based only smoke signatures, and salt-water dispersion signatures. The dimensionless detector activation times based on thermal signatures for the front arrival times showed similar trends.

Both the fire and salt-water predictions of the detector activation times matched very well for the both the ionization and photoelectric detectors for the various pool fire sizes. The detector activation increased with decreasing fire size. The front arrival and detector activation times for the different detectors at Bay 19 were attached in the **Appendix C Table 7**, **Table 8** and **Table 9**.

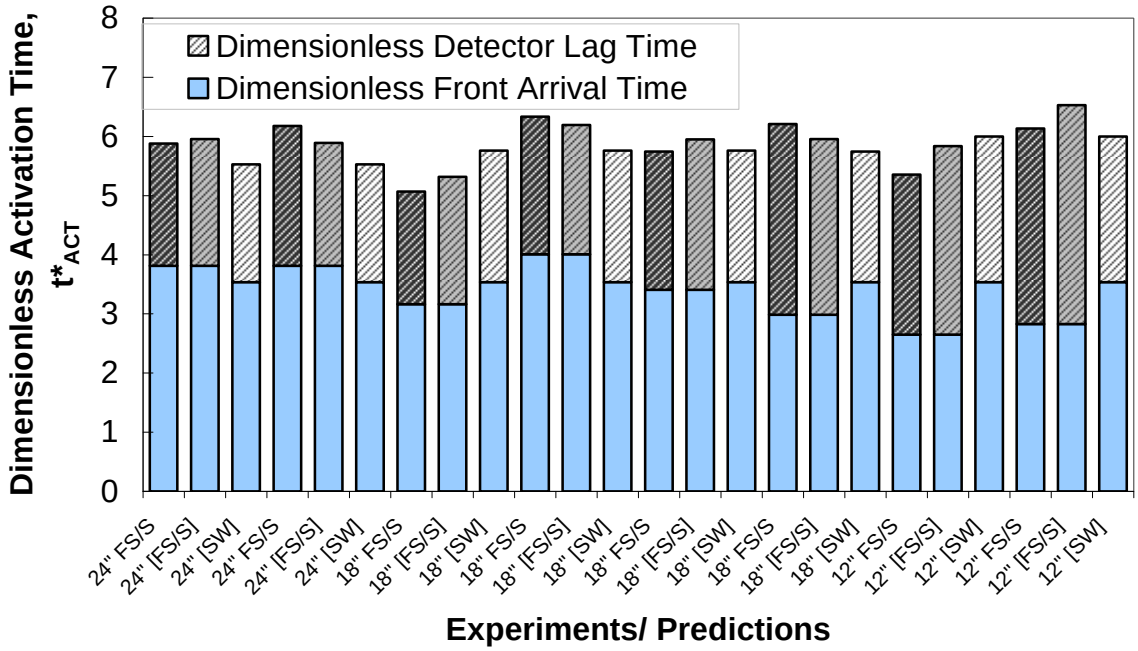

Figure 28 Dimensionless Detector Activation Times for Ionization Detector 1

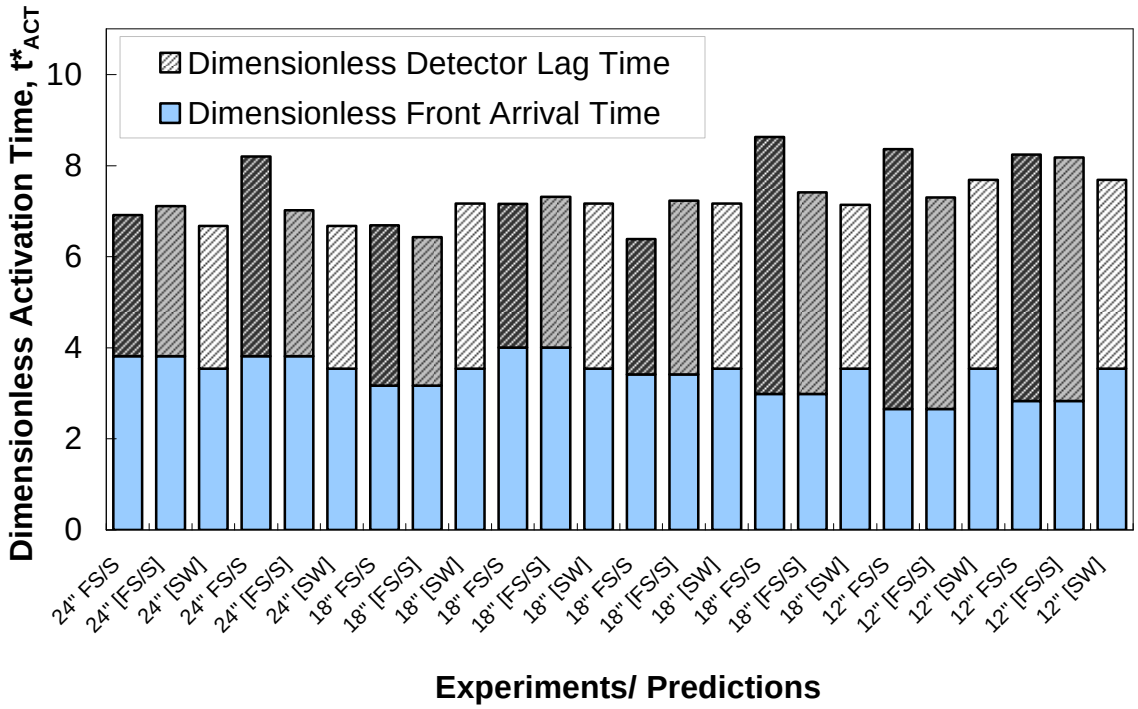

Figure 29 Dimensionless Detector Activation Times for Photoelectric Detector

3.8 Dispersion Characteristics at Bay 16, 17, 18 (Miter's Flow)

The dimensionless salt-water dispersion for the Bay 16, 17, 18 were extracted and shown in **Figure 30** for both the detector plane (PF12) and the ODM plane (PF10, PF11).

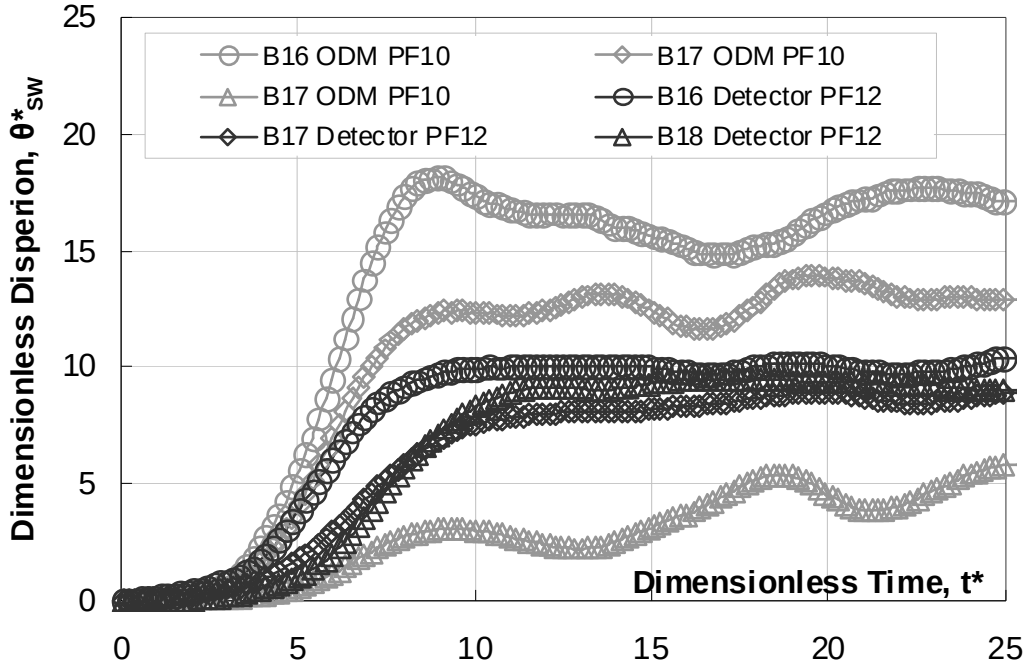

Figure 30 Dimensionless Saltwater Dispersion at Bay 16, 17, 18

The dispersion at the ODM plane was decreasing from Bay 16 to Bay 18, whereas the dispersion at the detector plane was relatively close. The discrete values at the ODM plane demonstrated the effect of the bays acting as reservoirs which caused the salt-water dispersion to be discontinuous. However, at the detector location which was nearer to the miter, the flow was connecting between the different bays at regions nearer to the miters. This agreed with the results from the PIV measurements as

showed in **Figure 12** where the resultant velocity magnitude was higher at nearer the miter' 'regions.

The front arrival times at the various bays demonstrated the sequence o flow whereby the flow reached the B16 ODM location, followed by the detector locations, and then B18 ODM locations. This presence of the miter had allowed for the flow to reach Bay 18 earlier at the detector location than if the flow had to travel from the B18 ODM location towards the detector locations without the miter's presence.

Chapter 4: Conclusion

The study successfully validated the use of salt-water analog modeling as an effective diagnostic, predictive and scaling tool for understanding fire dispersion by comparing the dispersion quantities in a beam-ceiling complex compartment for both the salt-water and fire experiments in the dimensionless domain through Froude scaling.

Salt-water modeling tools including the Blue dye, PIV and PLIF techniques were successfully carried out to

- validate the use of the large source injector with low initial momentum flux
- established the repeatability of the salt-water experiments at different flow rates
- develop the PIV and PLIF non-intrusive techniques to obtain quantitative measures such as the velocity and dispersion concentration of the flow within the complex geometry
- visualize and describe the flow due to the ceiling beams, the miters as well as the corridor openings qualitatively and quantitatively.

The conversion of the measurement data for both the salt-water and fire experiments to its dimensionless form were documented in the paper. The dimensionless variables at Bay 19 that were compared between the salt-water and fire experiments include

- time-evolution of the thermal dispersion for the burner and pool fires
- time-evolution of the smoke dispersion for the pool fires

- time-evolution of the salt-water dispersion
- steady-state dispersions
- front arrival times
- detector lag times, including velocity of the flow, detector characteristic length, and detector activation threshold
- detector activation times

Excellent agreement of the dimensionless dispersion quantities and front arrival times between the experiments validated the point-source scaling theory for salt-water modeling, and for different steady fire sources.

A dimensionless form for Heskestad's detector model was established to predict the detector lag times and activation times using fire and salt-water data. Excellent agreement between the predicted results and the fire experiments validated

- the applicability of the detector model to predict detector lag times for both ionization and photoelectric detectors, and that the dimensionless detector lag times increased with decreasing fire source strength, and
- the use of salt-water modeling as a predictive tool for the detector lag times and activation times.

The effects of the beams and miters on the flow of the ceiling jet were quantitatively discussed.

Further works to this paper may include

- carrying out additional PIV and PLIF measurements at other bay locations within the compartment to compare the dispersion profiles along the bay and along the corridor
- determining the effect of thermal boundary loss on salt-water modeling at the far-field
- establish the validity and limits of the detector model to predict lag times and activation times at far-field
- extending the salt-water scaling technique to compare dynamic fire source such as the wood crib fires and polyurethane foam fires
- flow visualization and measurement at the corridor openings
- using the quantitative results from the salt-water experiments to correlate the dispersion with the ceiling beam profiles

Appendix A: Details of the Beam configurations

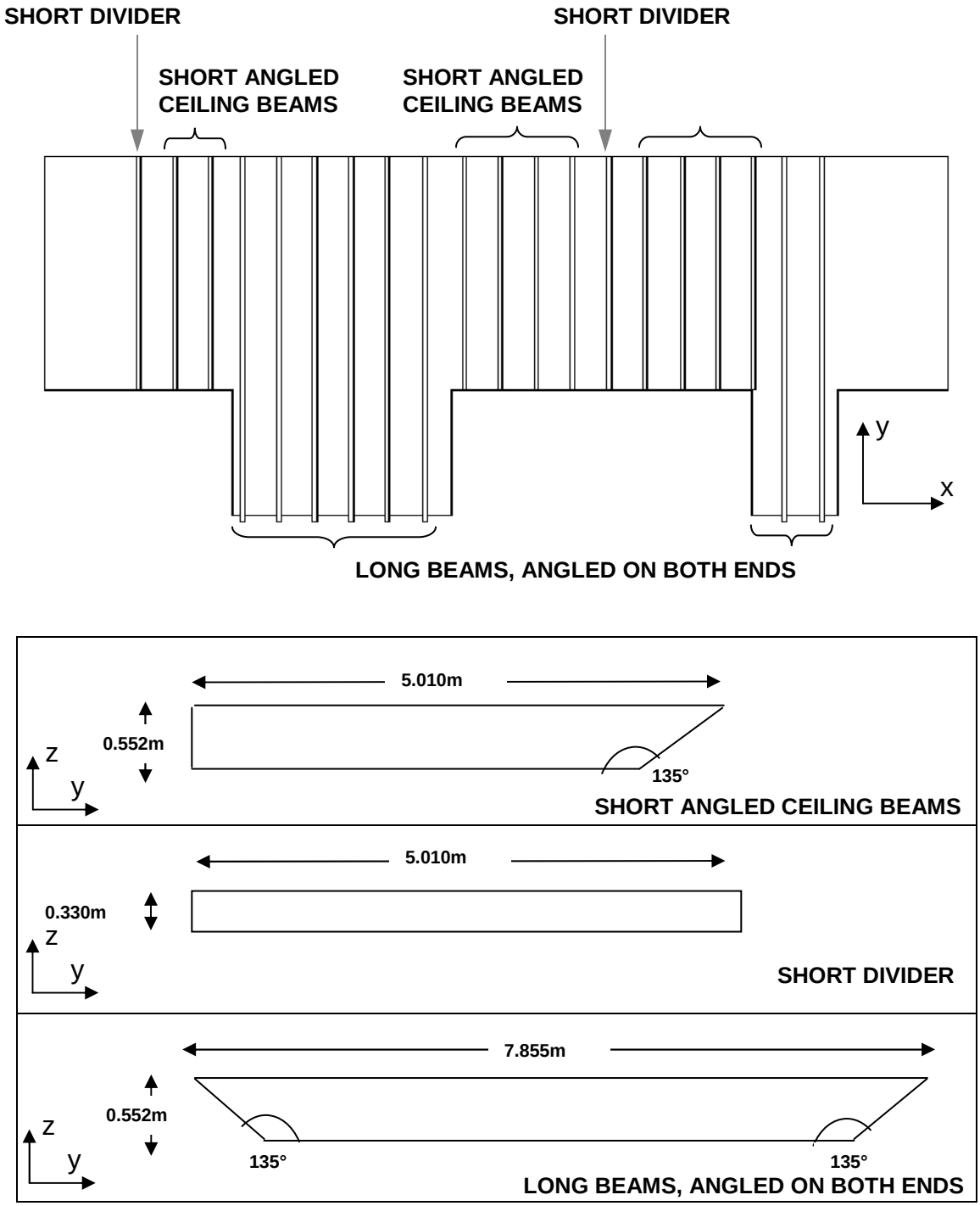

Figure 31 Dimensions of the beams

Appendix B: Details of the instrumentation for fire experiments

Instruments	Count	Bay locations
Thermocouple (Type K, Glass Ins., 28AWG wire)	63 48	B0 – B20 (along corridor) B2, B4, B10 (along bay)
Smoke Detector - Ionization (Model: Firex 4518) - Photoelectric (Model: Kidde PE120)	 8 4	 B2, B6, B13, B19 B2, B6, B13, B19
Optical Density Meter	4	B2, B6, B13, B19
HotWire Anemometer (Omega FMA-901-I-R)	4	B2, B6, B13, B19

Table 5 Summary of Instrumentation

Instrument	Location	X (m)	Y (m)	Z (m)
Thermocouple	B0-2in	0.384	0.761	4.383
Thermocouple	B0-6in	0.384	0.761	4.281
Thermocouple	B0-18in	0.384	0.761	3.972
Thermocouple	B1-2in	2.194	0.837	4.375
Thermocouple	B1-6in	2.194	0.837	4.272
Thermocouple	B1-18in	2.194	0.837	3.984
Thermocouple	B2-2in	2.778	0.777	4.353
Thermocouple	B2-6in	2.778	0.777	4.259
Thermocouple	B2-18in	2.778	0.777	3.959
Ionization 1	B2-Ion1-2m	2.719	1.283	4.361
Ionization 2	B2-Ion2-2m	2.913	1.280	4.361
Photoelectric	B2-PE-2m	2.806	1.262	4.353
Optical density meter	B2-ODM-2.5m	2.851	0.061	4.332
HotWire Anemometer	B2-1.8m	2.989	0.773	4.346
Thermocouple	B3-2in	3.631	0.821	4.365
Thermocouple	B3-6in	3.631	0.821	4.269
Thermocouple	B3-18in	3.631	0.821	3.968
Thermocouple	B4-2in	4.345	0.835	4.362
Thermocouple	B4-6in	4.345	0.835	4.266
Thermocouple	B4-18in	4.345	0.835	3.970
Thermocouple	B5-2in	5.061	0.812	4.359
Thermocouple	B5-6in	5.061	0.812	4.263
Thermocouple	B5-18in	5.061	0.812	3.953
Thermocouple	B6-2in	5.514	0.783	4.361
Thermocouple	B6-6in	5.514	0.783	4.263
Thermocouple	B6-18in	5.514	0.783	3.953
Ionization 1	B6-Ion1-2m	5.543	1.253	4.348
Ionization 2	B6-Ion-2-2m	5.866	1.239	4.348
Photoelectric	B6-PE-2m	5.737	1.238	4.344
Optical density meter	B6-ODM-2.5m	5.750	0.053	4.228
HotWire Anemometer	B6-1.8m	5.866	0.759	4.356

Thermocouple	B7-2in	6.471	0.797	4.351
Thermocouple	B7-6in	6.471	0.797	4.261
Thermocouple	B7-18in	6.471	0.797	4.051
Thermocouple	B8-2in	7.172	0.786	4.349
Thermocouple	B8-6in	7.172	0.786	4.253
Thermocouple	B8-18in	7.172	0.786	3.956
Thermocouple	B9-2in	7.877	0.792	4.363
Thermocouple	B9-6in	7.877	0.792	4.261
Thermocouple	B9-18in	7.877	0.792	3.980
Thermocouple	B10-2in	8.578	0.791	4.367
Thermocouple	B10-6in	8.578	0.791	4.264
Thermocouple	B10-18in	8.578	0.791	3.974
Thermocouple	B11-2in	9.331	0.797	4.363
Thermocouple	B11-6in	9.331	0.797	4.264
Thermocouple	B11-18in	9.331	0.797	3.969
Thermocouple	B12-2in	10.009	0.761	4.372
Thermocouple	B12-6in	10.009	0.761	4.279
Thermocouple	B12-18in	10.009	0.761	3.983
Thermocouple	B13-2in	10.516	0.820	4.374
Thermocouple	B13-6in	10.516	0.820	4.279
Thermocouple	B13-18in	10.516	0.820	3.977
Ionization 1	B13-Ion1-2m	10.524	1.261	4.359
Ionization 2	B13-Ion2-2m	10.834	1.258	4.358
Photoelectric	B13-PE-2m	10.680	1.284	4.356
Optical density meter	B13-ODM-2.5m	10.761	0.036	4.337
HotWire Anemometer	B13-1.8m	10.854	0.763	4.357
Thermocouple	B14-2in	11.413	0.814	4.373
Thermocouple	B14-6in	11.413	0.814	4.282
Thermocouple	B14-18in	11.413	0.814	3.988
Thermocouple	B15-2in	12.134	0.732	4.379
Thermocouple	B15-6in	12.134	0.732	4.276
Thermocouple	B15-18in	12.134	0.732	3.990
Thermocouple	B16-2in	12.854	0.783	4.359
Thermocouple	B16-6in	12.854	0.783	4.257
Thermocouple	B16-18in	12.854	0.783	3.989
Thermocouple	B17-2in	13.571	0.740	4.366
Thermocouple	B17-6in	13.571	0.740	4.269
Thermocouple	B17-18in	13.571	0.740	3.974
Thermocouple	B18-2in	14.285	0.759	4.372
Thermocouple	B18-6in	14.285	0.759	4.267
Thermocouple	B18-18in	14.285	0.759	3.970
Thermocouple	B19-2in	14.832	0.772	4.367
Thermocouple	B19-6in	14.832	0.772	4.279
Thermocouple	B19-18in	14.832	0.772	3.984
Ionization 1	B19-Ion1-2m	14.815	1.359	4.361
Ionization 2	B19-Ion2-2m	15.015	1.356	4.362
Photoelectric	B19-PE-2m	14.920	1.354	4.360
Optical density meter	B19-ODM-2.5m	14.960	-0.015	4.332

HotWire Anemometer	B19-1.8m	15.178	0.765	4.356
Thermocouple	B20-2in	16.335	0.772	4.382
Thermocouple	B20-6in	16.335	0.772	4.279
Thermocouple	B20-18in	16.335	0.772	3.978
Instrument	**Location**	**X (m)**	**Y (m)**	**Z (m)**
Thermocouple	B2-1ft	-9.956	2.51	4.134
Thermocouple	B2-2ft	-9.956	2.203	4.134
Thermocouple	B2-3ft	-9.956	1.919	4.134
Thermocouple	B2-4ft	-9.956	1.597	4.134
Thermocouple	B2-5ft	-9.956	1.287	4.134
Thermocouple	B2-6ft	-9.956	1.009	4.134
Thermocouple	B2-7ft	-9.956	0.694	4.134
Thermocouple	B2-8ft	-9.956	0.395	4.134
Thermocouple	B2-9ft	-9.956	0.101	4.134
Thermocouple	B2-10ft	-9.956	-0.215	4.134
Thermocouple	B2-11ft	-9.956	-0.496	4.134
Thermocouple	B2-12ft	-9.956	-0.823	4.134
Thermocouple	B2-13ft	-9.956	-1.104	4.134
Thermocouple	B2-14ft	-9.956	-1.402	4.134
Thermocouple	B2-15ft	-9.956	-1.722	4.134
Thermocouple	B2-16ft	-9.956	-1.963	4.134
Thermocouple	B4-1ft	-8.528	2.530	4.119
Thermocouple	B4-2ft	-8.528	2.205	4.119
Thermocouple	B4-3ft	-8.528	1.913	4.119
Thermocouple	B4-4ft	-8.528	1.603	4.119
Thermocouple	B4-5ft	-8.528	1.338	4.119
Thermocouple	B4-6ft	-8.528	1.023	4.119
Thermocouple	B4-7ft	-8.528	0.694	4.119
Thermocouple	B4-8ft	-8.528	0.425	4.119
Thermocouple	B4-9ft	-8.528	0.120	4.119
Thermocouple	B4-10ft	-8.528	-0.204	4.119
Thermocouple	B4-11ft	-8.528	-0.479	4.119
Thermocouple	B4-12ft	-8.528	-0.803	4.119
Thermocouple	B4-13ft	-8.528	-1.117	4.119
Thermocouple	B4-14ft	-8.528	-1.395	4.119
Thermocouple	B4-15ft	-8.528	-1.696	4.119
Thermocouple	B4-16ft	-8.528	-1.989	4.119
Thermocouple	B10-1ft	-4.240	2.488	4.064
Thermocouple	B10-2ft	-4.240	2.192	4.064
Thermocouple	B10-3ft	-4.240	1.915	4.064
Thermocouple	B10-4ft	-4.240	1.563	4.064
Thermocouple	B10-5ft	-4.240	1.293	4.064
Thermocouple	B10-6ft	-4.240	0.982	4.064
Thermocouple	B10-7ft	-4.240	0.673	4.064
Thermocouple	B10-8ft	-4.240	0.386	4.064
Thermocouple	B10-9ft	-4.240	0.085	4.064

Thermocouple	B10-10ft	-4.240	-0.249	4.064
Thermocouple	B10-11ft	-4.240	-0.559	4.064
Thermocouple	B10-12ft	-4.240	-0.851	4.064
Thermocouple	B10-13ft	-4.240	-1.193	4.064
Thermocouple	B10-14ft	-4.240	-1.430	4.064
Thermocouple	B10-15ft	-4.240	-1.743	4.064
Thermocouple	B10-16ft	-4.240	-1.995	4.064

Table 6 Locations of the instrumentation

Appendix C: Results on front arrival times, detector lag times, and detector activation times.

Experiment ID	4414	4412	4420	4421	4415	4416	4418	4419
Pool Fires	24”	24”	18”	18”	18”	18”	12”	12”
(A) Fire experimental results								
$t_{FA\ (thermal)}$ [s]	*15*	*14*	*16*	*21*	*18*	*18*	*22*	*22*
$t_{FA\ (smoke)}$ [s]	*14*	*14*	*15*	*19*	*16*	*14*	*15*	*16*
t_{lag} [s]	*7*	*8*	*9*	*11*	*11*	*15*	*18*	*22*
t_{ACT} [s]	*21*	*22*	*24*	*30*	*27*	*29*	*33*	*38*
(B) Dimensionless fire experimental results								
$t^*_{FA\ (thermal)}$	*4.1*	*3.8*	*3.4*	*4.4*	*3.8*	*3.8*	*3.9*	*3.9*
$t^*_{FA\ (smoke)}$	*3.8*	*3.8*	*3.2*	*4.0*	*3.4*	*3.0*	*2.7*	*2.8*
$t^*_{lag\ (Fire\ Experiment)}$	*1.9*	*2.2*	*1.9*	*2.3*	*2.3*	*3.2*	*3.2*	*3.9*
$t^*_{ACT\ (Fire\ Experiment)}$	*5.7*	*6.0*	*5.1*	*6.3*	*5.7*	*6.2*	*5.8*	*6.7*
(C) Prediction based on smoke dispersion for fire experiments								
$t^*_{FA\ (smoke)}$	*3.8*	*3.8*	*3.2*	*4.0*	*3.4*	*3.0*	*2.7*	*2.8*
$t^*_{lag\ (Prediction\ -Fire)}$	*2.1*	*2.1*	*2.2*	*2.2*	*2.5*	*3.0*	*3.2*	*3.7*
$t^*_{ACT\ (Fire\ Experiment)}$	*5.9*	*5.9*	*5.3*	*6.2*	*6.0*	*6.0*	*5.8*	*6.5*
(D) Prediction based on salt-water dispersion								
$t^*_{FA\ (SW)}$	*3.5*	*3.5*	*3.5*	*3.5*	*3.5*	*3.5*	*3.5*	*3.5*
$t^*_{lag\ (Prediction\ –\ SW)}$	*2.0*	*2.0*	*2.2*	*2.2*	*2.2*	*2.2*	*2.5*	*2.5*
$t^*_{ACT\ (SW)}$	*5.5*	*5.5*	*5.7*	*5.7*	*5.7*	*5.7*	*6.0*	*6.0*

Table 7 Dimensionless Front Arrival, Detector lag and Activation Times for ionization detector 1

Experiment ID	4414	4412	4420	4421	4415	4416	4418	4419
Pool Fires	24”	24”	18”	18”	18”	18”	12”	12”
(A) Fire experimental results								
$t_{FA\ (thermal)}$ [s]	*15*	*14*	*16*	*21*	*18*	*18*	*22*	*22*
$t_{FA\ (smoke)}$ [s]	*14*	*14*	*15*	*19*	*16*	*14*	*15*	*16*
t_{lag} [s]	*12*	*17*	*19*	*17*	*16*	*30*	*38*	*36*
t_{ACT} [s]	*26*	*31*	*34*	*36*	*32*	*44*	*53*	*52*
(B) Dimensionless fire experimental results								
$t^*_{FA\ (thermal)}$	*4.1*	*3.8*	*3.4*	*4.4*	*3.8*	*3.8*	*3.9*	*3.9*
$t^*_{FA\ (smoke)}$	*3.8*	*3.8*	*3.2*	*4.0*	*3.4*	*3.0*	*2.7*	*2.8*
$t^*_{lag\ (Fire\ Experiment)}$	*3.3*	*4.6*	*4.0*	*3.6*	*3.4*	*6.4*	*6.7*	*6.4*
$t^*_{ACT\ (Fire\ Experiment)}$	*7.1*	*8.4*	*7.2*	*7.6*	*6.8*	*9.4*	*9.4*	*9.2*
(C) Prediction based on smoke dispersion for fire experiments								
$t^*_{FA\ (smoke)}$	*3.8*	*3.8*	*3.2*	*4.0*	*3.4*	*3.0*	*2.7*	*2.8*
$t^*_{lag\ (Prediction\ -Fire)}$	*3.5*	*3.4*	*3.5*	*3.6*	*4.2*	*4.9*	*5.2*	*6.0*
$t^*_{ACT\ (Fire\ Experiment)}$	*7.3*	*7.2*	*6.7*	*7.6*	*7.6*	*7.8*	*7.8*	*8.9*
(D) Prediction based on salt-water dispersion								
$t^*_{FA\ (SW)}$	*3.5*	*3.5*	*3.5*	*3.5*	*3.5*	*3.5*	*3.5*	*3.5*
$t^*_{lag\ (Prediction\ –\ SW)}$	*3.3*	*3.3*	*3.6*	*3.6*	*3.7*	*3.6*	*4.0*	*4.0*
$t^*_{ACT\ (SW)}$	*6.8*	*6.8*	*7.1*	*7.1*	*7.2*	*7.1*	*7.5*	*7.5*

Table 8 Dimensionless Front Arrival, Detector lag and Activation Times for photoelectric detector

Experiment ID	4414	4412	4420	4421	4415	4416	4418	4419
Pool Fires	24”	24”	18”	18”	18”	18”	12”	12”
(A) Fire experimental results								
$t_{FA\ (thermal)}$ [s]	*15*	*14*	*16*	*21*	*18*	*18*	*22*	*22*
$t_{FA\ (smoke)}$ [s]	*14*	*14*	*15*	*19*	*16*	*14*	*15*	*16*
t_{lag} [s]	*6*	*7*	*23*	*22*	*9*	*10*	*15*	*19*
t_{ACT} [s]	*20*	*21*	*38*	*41*	*25*	*24*	*30*	*35*
(B) Dimensionless fire experimental results								
$t^*_{FA\ (thermal)}$	*4.1*	*3.8*	*3.4*	*4.4*	*3.8*	*3.8*	*3.9*	*3.9*
$t^*_{FA\ (smoke)}$	*3.8*	*3.8*	*3.2*	*4.0*	*3.4*	*3.0*	*2.7*	*2.8*
$t^*_{lag\ (Fire\ Experiment)}$	*1.6*	*1.9*	*4.9*	*4.6*	*1.9*	*2.1*	*2.7*	*3.4*
$t^*_{ACT\ (Fire\ Experiment)}$	*5.4*	*5.7*	*8.0*	*8.6*	*5.3*	*5.1*	*5.3*	*6.2*
(C) Prediction based on smoke dispersion for fire experiments								
$t^*_{FA\ (smoke)}$	*3.8*	*3.8*	*3.2*	*4.0*	*3.4*	*3.0*	*2.7*	*2.8*
$t^*_{lag\ (Prediction\ -Fire)}$	*2.1*	*2.1*	*2.2*	*2.2*	*2.5*	*3.0*	*3.2*	*3.7*
$t^*_{ACT\ (Fire\ Experiment)}$	*5.9*	*5.9*	*5.3*	*6.2*	*6.0*	*6.0*	*5.8*	*6.5*
(D) Prediction based on salt-water dispersion								
$t^*_{FA\ (SW)}$	*3.5*	*3.5*	*3.5*	*3.5*	*3.5*	*3.5*	*3.5*	*3.5*
$t^*_{lag\ (Prediction\ –\ SW)}$	*2.0*	*2.0*	*2.2*	*2.2*	*2.2*	*2.2*	*2.5*	*2.5*
$t^*_{ACT\ (SW)}$	*5.5*	*5.5*	*5.7*	*5.7*	*5.7*	*5.7*	*6.0*	*6.0*

Table 9 Dimensionless Front Arrival, Detector lag and Activation Times for ionization detector 2

Bibliography

[1] *R.L. Alpert, "Fire Induced Turbulent Ceiling-Jet," Factory Mutual Research Corporation, Norwood MA, FMRC Serial No.19722-2, pp 35(1971).*

[2] *R.L. Alpert, "Calculations of Response Time of Ceiling Mounted Fire Detecors" Fire Technology, 8, 3, pp 181-195 (1972).*

[3] *G. Heskestad and M. A. Delichatsios. Environments of Fire Detectors – Phase I: Effect of Fire Size, Ceiling Height and Material, Volume I & II. Measurements & Analysis. Nbs-gcr-77-86 & Nbs-gcr-77-95, National Institute of Standards and Technology (1977).*

[4] *G. Heskestad, "Physical Modeling of Fire," Journal of Fire & Flammability, 6, p. 253 (1975).*

[5] *G. Heskestad, "Generalized Characteristics of Smoke Entry and Response for Products-of-Combustion Detectors," in Proceedings, 7th International Conference on Problems of Automatic Fire Detection, Rheinish-Westfalischen Technischen Hochschule, Aachen, Germany (1975).*

[6] *K.D. Steckler, H.R. Baum, and J.G. Quintiere, " Salt Water Modeling of Fire Induced Flows in Multi-Compartment Enclosures," NBSIR 86-3327, Gaithersburg, MD: National Bureau of Standards (1986).*

[7] *A.A. Kelly, "Examination of Smoke Movement in a Two-Story Compartment Using Salt Water and Computational Fluid Dynamics Modeling," M.S. Thesis, Dept. Fire Protection Engineering, University of Maryland, College Park, MD (2001).*

[8] S.P. Jankiewicz "Predicting Smoke Detector Response Using a Quantitative Salt-Water *Modeling Technique", M.S. Thesis, Dept. Fire Protection Engineering, University of Maryland, College Park (2004)*

[9] *M. Delichatsios, ''The Flow of Fire Gases Under a Beamed Ceiling'', Combustion and Flame, 43, pp 1 (1981).*

[10] *C. Koslowski and V. Motevalli, ''Effect of Beams on Ceiling Jet Behavior and Heat Detector Operation'', Journal of Fire Protection Engineering, 5, 3, pp. 97–112 (1993).*

[11] *G.P. Forney, W.D. Davis and J.H. Klote, "Simulating the Effect of Beamed Ceilings on Smoke Flow. Part 1. Comparison of Numerical and Experimental Results." NISTIR 4994; pp 24 (1992).*

[12] *C. Koslowski and V. Motevalli, ''Behavior of a 2-Dimensional Ceiling Jet Flow: A Beamed Ceiling Configuration''. in T. Kashiwagi (ed.), Fire Safety Science – Proceedings of the Fourth International Symposium. International Association of Fire Safety Science, pp 469–480 (1994).*

[13] *J.G. Quintiere, "Scaling Applications in Fire Research", Fire Safety Journal, 15: p. 3-29 (1989).*

[14] *P.H. Thomas et al., "Investigation into the flow of hot gases in roof venting", F.R. Technical Paper No 7, Department of Scientific and Industrial Research and Fire Offices' Committee Joint fire Research Organization, London (1963).*

[15] *E.E. Zukoski, "Prediction of Smoke Movement in Buildings," California Institute of Technology, Pasadena, CA (1978).*

[16] *H.P. Zhang, W.C. Fan, T.J. Shields and G. Silock," Salt Water Simulation of the Movement Characteristics of Smoke and Induced Air in a Room-Corridor Building", Journal of Applied Fire Science, 7, 4, pp. 361-385 (1977-1998).*

[17] *J.M. Clement and C.M. Fleischman, "Experimental Verification of the Fire Dynamics Simulator Hydrodynamic Model", Fire Safety Science – Proceedings of the Seven International Symposium, pp. 839-851 (2000).*

[18] *E.L. Young "Wind-driven Plume Dispersion Near a Building", M.S. Thesis, Dept. Fire Protection Engineering, University of Maryland, College Park (2008)*

[19] *X. Yao, T. Ma, A.W. Marshall, A. Trouve, "Mixing and Turbulent Transport in Unconfined and Impinging Plumes", Proceedings of the InterFlam International Symposium, Edinburgh, Scotland (2004)*

[20] *X. Yao, T. Ma, A.W. Marshall, "Quantitative Salt-water Modeling of Fire Induced Flow", Fire Safety Journal, 41, 7, pp. 497-508 (2006).*

[21] *X. Yao, T. Ma, and A.W. Marshall, "Characterizing of Ceiling Jet Dynamics With Salt-water Modeling", Fire Safety Science - Proceedings of the 8th International Symposium, International Association of Fire Safety Science, Beijing, China (2005).*

[22] *F. Taylor, "The Automatic Control of Fire," Quarterly of the National Fire Protection Association, pp149-162 (1912).*

[23] *G. Heskestad and M.A. Delichatsios,"Environments of Fire Detectors – Phase II: Effect of Ceiling Configuration, Volume I & II – Measurements and Analysis," NBS-GCR-78-128 & NBS-GCR-78-129, National Institute of Standards and Technology (1978).*

[24] *G. Heskestad, "Model Study of ESFR Sprinkler Response Under Beamed Ceilings", Technical Report, FMRC J.I. 0N0E3.RU. Factory Mutual Research Corporation, Norwood, MA (1987).*

[25] *Motevalli V., Zheng P.Y., "Steady State Ceiling Jet Behavior under an Unconfined Ceiling with Beams" Fire Technology, 44, 97-112 (2008).*

[26] *G. Forney, R. Bukowski, and W. Davis, "Field Modeling: Effects of Flat Beamed Ceilings on Detector and Sprinkler Response, Technical Report Year 1", Fire Protection Research Foundation, Quincy, MA, 1993.*

[27] *D. O'Connor et al., "Smoke Detector Performance for Level Ceilings with Deep Beams and Deep Beam Pocket Configurations", Fire Protection Research Foundation, Quincy, MA, (2006).*

[28] *J. Floyd, "Evaluating Smoke Detector Spacing Requirements for Parallel Beamed Hallways and Sloped Ceilings", Fire Protection Research Foundation, Quincy, MA, (2008).*

[29] *C.L. Mealy, "Experimental Validation of Smoke Detector Spacing Requirements", Fire Protection Research Foundation, Quincy, MA, (2008).*

[30] *D. Evans, D. Stroup, "Methods to Calculate the Response Time of Heat and Smoke Detectors Installed Below Large Unobstructed Ceilings", NBSIR 85-3167, National Bureau of Standards, Gaithersburg, MD (1985).*

[31] *F.W. Mowrer, and J. Friedman, "Experimental Investigation of Heat and Smoke Detector Response", Proceedings of Fire Suppression and Detection Research Application Symposium, pp. 256 – 264 (1998).*

[32] *J.A. Geiman, "Evaluation of Smoke Detector Response Estimation Methods", M.S. Thesis, University of Maryland Department of Fire Protection Engineering (2003).*

[33] *J.A. Geiman, and D.T. Gottuk, "Alarm Thresholds for Smoke Detector Modeling," Fire Safety Science – Proceedings of the 7th International Symposium, International Association for Fire Safety Science, pp. 197 – 208 (2003).*

[34] *J. Bj□rkman et al., "Determination of Dynamic Model Parameters of Smoke Detectors", Fire Safety Journal. 37, p. 395-407 (1992).*

[35] T. Cleary, A. Chernovsky, W. Grosshandler, and M. Anderson, "Particulate Lag Entry in Spot-Type Smoke Detectors," Fire Safety Science – Proceedings of the 6th International Symposium, International Association for Fire Safety Science, pp. 779 –780 (2000).

[36] Heskestad, G., "Virtual origins of fire plumes," Fire Safety Journal, 5, pp. 109–14 (1983).

[37] B.R. Morton, G.I. Taylor, and J.S. Tuner, "*Turbulent Gravitational Correction From Maintained and Instantaneous Sources,"* Proc. R. Soc. Lond. A, **234**, pp.1-23 (1956).

[38] E.E. Zukosiki, T. Kubota, and B. Cetegen, "Entrainment in Fire Plumes," Fire Safety Journal, 3, pp. 107-121 (1980/1981).

[39] Z.T. Dai, L.-K., and G.M. Faeth, "Structure of Round, Fully Developed, Buoyant Turbulent Plumes," Journal of Heat Transfer, 116, pp. 409-417 (1994).

[40] A. Tewarson, "Generation of Heat and Chemical Compounds in Fires", SFPE Handbook of Fire Protection Engineering, 3rd edition, National Fire Protection Association, Quincy, MA, 2002.

[41] G.W. Mulholland et al., "Proceedings of the Second International Symposium on Fire Safety Science" Hemisphere, New York, p. 347 (1989).